POLITECNICO
MILANO 1863

DEPARTMENT OF ELECTRONICS, INFORMATION AND BIOENGINEERING
DOCTORAL PROGRAM IN BIOENGINEERING

STATISTICAL SHAPE MODELS BASED 2D/3D REGISTRATION METHODS FOR KNEE ORTHOPAEDIC SURGERY

Doctoral Dissertation of:
Marta Valenti

Supervisor:
Prof. Elena De Momi
Prof. Guoyan Zheng

Tutor:
Prof. Enrico Caiani

The Chair of the Bioengineering Doctoral Program:
Prof. Andrea Aliverti

2015 – XXVIII Cycle

Alla mia famiglia

Abstract

In orthopaedic surgery, and in case of Total Knee Arthroplasty (TKA) for osteoarthritic subjects, planning of the intervention is of fundamental importance. The insertion of the prosthetic components is extremely delicate because the deformations induced by the osteophytes must be resected and at the same time the mechanical axis of the leg must be corrected. The size of the implant and the plane of resection are estimated through a standing X-ray projection that covers the whole leg. This view gives a hint on the direction of the mechanical axis that must be restored, but cannot evaluate how the kinematics of the knee is influenced by the insertion. The possibility to check the pre-operative kinematic of the knee under weight bearing conditions, in order to evaluate tension of the ligaments and the distance between the bones, would be of great importance for the success of the intervention, giving to the surgeon the possibility to check the bone's motion before entering in the surgery room. This evaluation is currently intraoperatively performed by the surgeon, who performs passive movements of the joint to check the correct placement of the prosthetic components, although the conditions are not similar to the real stress applied during everyday life, as weight and muscles strengths are missing.

The use of fluoroscopic sequences is common in clinics to rapidly evaluate the knee kinematics. These fast and low dose X-ray images allow an accurate visualization of the bone movements without the invasiveness typical of other methodologies. Knee motion analysis is cur-

rently done manually superimposing the shape obtained from Computed Tomography (CT) or Magnetic Resonance Imaging (MRI) on the fluoroscopic set acquired. The surgeon evaluates the projection of the shape on the image plane and through further approximations defines the best pose of the model onto the images. This procedure occupies the surgeon for a long time, and is affected by operator inaccuracies. A completely automatic algorithm would solve the challenge, relieving the surgeon from the duty of detecting the correct pose and allowing a fast and accurate 2D/3D registration. Eventually, the shape could also be derived from a Statistical Shape Model (SSM), in order to reduce costs and radiation doses that would be higher with a subject-specific shape derived from CT or MRI.

The work herein presented shows two alternative methods to perform 2D/3D registration for femur kinematics estimation, starting from a set of fluoroscopic images and a SSM. Both algorithms allow the surgeon to have a more complete and functional evaluation of the knee performance under weight bearing conditions, that is essential for some type of operations, such as osteoarthritis and patellofemoral pain.

The thesis begins with the description of a new method for SSM creation, based on the Minimum Description Length (MDL) algorithm. SSMs are currently used in orthopaedic surgery to allow accurate positioning of prosthetic components through bone morphing and to assess the correct post-operative follow up by virtually reconstructing the surgical site. Focusing on computer assisted TKA applications, a new approach for establishing landmark correspondence of 3D shapes is proposed, to build SSMs of anatomical structures of the knee joint. The method is based on landmark correspondence by MDL and introduces a new constraint on local geometric similarity. This local linear regularization ensures that the local shape geometry of corresponding landmarks on different shapes is similar. The method was tested building SSMs of three anatomical structures from MRI images of knees, namely femur, patella and tibia. Compared with the original method using only the MDL criterion, this new approach shows significant improvement both qualitatively and quantitatively. The landmarks are in fact better distributed on the shape surface, and can more accurately represent the underlying shapes.

The new SSM is the basis for the development of a 2D/3D registration algorithm for knee kinematics reconstruction. Starting from the acquisition of two calibrated fluoroscopic images, taken at different flexion-extension angles, the algorithm performs a feature based non-rigid registration. The projection of the model's silhouette and the contour extracted from the fluoroscopic image are matched using a one-to-many correspondence based on a nearest neighbour approach. To avoid local minima, the optimization is inserted in a Genetic Algorithm (GA), that solves the issues of the suboptimal results but slows down the time for the solution. The proposed approach was evaluated on 3 sets of digitally reconstructed radiographic images of osteoarthritic patients. Using the estimated shape, rather than that calculated from CT, significantly reduces the pose accuracy, but still has reasonably good results (angle errors around 2 degrees, translation around 1.5mm). The obtained results proved to be comparable with the literature, even if our trials were done using pathological femurs. Although accurate, the algorithm is very slow and it took a few hours for every femur pose to be properly reconstructed.

To overcome this limitation, a new algorithm based on Gaussian Mixture Model (GMM) is implemented. It is based on the definition of Gaussian mixture, so that each point of the 3D shape used for reconstruction is considered a mixture of Gaussian Probability Density Function (PDF). Using a Maximum Likelihood Estimation (MLE) approach, the most probable position of the shape in the 3D space is obtained. The algorithm was evaluated using Digitally Reconstructed Radiographs (DRRs) of both healthy and diseased subjects, with a CT extracted shape and a SSM as the 3D model. In vivo tests were done with fluoroscopically acquired images and subject specific CT shapes. The results obtained are in line with the literature, but the computational time is substantially reduced. This method proved to be accurate and fast, providing to the surgeon an efficient tool to check the pre-operatory kinematics of the knee in a virtual 3D environment.

Both the algorithms described show a millimeter accuracy, comparable with the results obtained in literature. The novelty of the GMM approach opens the way to a fast and accurate kinematic pose reconstruction for surgery planning, increasing the performance of the operations and reducing hospitalization costs. The registration is inserted in a clini-

cal routine already performed: it does not imply additional examinations of the patient and provides a valid external help to the surgeon.

Ringraziamenti

Un grazie va a chi mi ha aiutato in questi 3 anni di lavoro, tutto il team del NEARLab, in particolar modo il professor Ferrigno e l'ing. De Momi, la mia famiglia e i miei amici.

I would also like to thank all the IPMI group, and in particular professor Zheng and professor Nolte, who gave me the possibility to work under their supervision.

Il miglior ringraziamento va a mio marito, che mi ha sopportato in questi anni e mi ha sempre spronato a lavorare al meglio delle mie possibilità.

Contents

Ringraziamenti **V**

1 Clinical problem **3**
1.1 Knee osteoarthritis 3
1.2 Surgery planning 5
1.3 State of the art 7
1.4 Aim of the work and thesis structure 9

2 Statistical Shape Model creation **11**
2.1 Introduction 11
2.2 The Proposed Method 13
2.2.1 Problem Formulation 13
2.2.2 Miminum Description Length cost function 15
2.2.3 Local Linear Regularization cost function 15
2.2.4 Optimization Process 16
2.3 Experiments 18
2.3.1 Bipartite matching difference measure 19
2.3.2 Wald-Wolfowitz test 20
2.3.3 Results 20
2.3.4 Discussion 20
2.4 Conclusions 22

3 Femur kinematics registration based on Genetic Algorithms **23**
3.1 State of the art 23

3.2 Methods 26
3.2.1 Statistical Shape Model (SSM) creation 26
3.2.2 Shape pose initialization 28
3.2.3 Femur tracking 31
3.2.4 Validation 33
3.3 Results 37
3.4 Discussion 38

4 Femur kinematics registration based on Gaussian Mixture Models 43
4.1 Introduction 43
4.2 Materials and methods 45
4.2.1 Datasets 45
4.2.2 Registration 47
4.2.3 Validation protocol 53
4.3 Results 58
4.4 Discussion 59

5 Conclusions 65

Bibliography 69

List of Figures

1.1 Representation of knee osteoarthritis 4
1.2 Knee implant representation 5
1.3 Rendering of a biplanar acquisition setup 8
1.4 Comparison between a fluoroscopic image and a DRR . . 8
1.5 Structure of the thesis 10

2.1 Landmarks definition 12
2.2 Description of the spherical parametrization 14
2.3 Same patella mesh processed with two different values of α 21
2.4 Same tibia mesh processed with two different values of α . 21

3.1 Flowchart of the GA based algorithm. 27
3.2 Definition of the landmark pose in the 3D space 30
3.3 Schematic of the reference frames involved 30
3.4 Definition of the contour edge 32
3.5 Objective function 32
3.6 DRR creation - view angles 35
3.7 DRR creation - flexion angles 36
3.8 Similarity between CT and SSM mesh 37
3.9 Rotation precision 38
3.10 Translation precision 39

4.1 Flowchart of the GMM based algorithm. 46
4.2 Description of silhouette projection 48

4.3 DRR creation 57
4.4 Contour points and Silhouette 58
4.5 Translation and rotation error for S_0 60
4.6 Translation and rotation error for S_1, S_2, S_3 61
4.7 Edge to surface index evaluation for S_1, S_2, S_3 62
4.8 Edge to surface index evaluation for S_{1-7} 62

List of Tables

2.1 Schema of the three different experiments done 18
2.2 SSM creation results achieved 21

3.1 Pros and Cons of the different methods to acquire knee kinematics 24
3.2 Mesh comparison statistical parameters: distances from point to surface represented as mean and standard deviation 37

4.1 Subject description 56

Acronyms

BMI Body Mass Index

CAS Computer Assisted Surgery

CT Computed Tomography

DRR Digitally Reconstructed Radiograph

ECM Expectation Conditional Maximization

EM Expectation Maximization

E2S Edge to Surface

GA Genetic Algorithm

GMM Gaussian Mixture Model

LLR Local Linear Regularization

LMS Least Mean Squares

MDL Minimum Description Length

ML Maximum Likelihood

MLE Maximum Likelihood Estimation

MRI Magnetic Resonance Imaging

OA OsteoArthritis

OECD Organization for economic cooperation and development

PCA Principal Component Analisys

PDF Probability Density Function

RF Reference Frame

RMSE Root Mean Square Error

RSA Radio Stereometric Analysis

SSM Statistical Shape Model

TKA Total Knee Arthroplasty

CHAPTER 1

Clinical problem

1.1 Knee osteoarthritis

Knee OsteoArthritis (OA) is one of the most spread diseases of aged people and it is in absolute the most common form of arthritis [29]. It can be defined as a degenerative pathology that involves joints and in particular cartilages. Even if it can affect every joint of the human body, it occurs more often in the knee, hip, fingers and neck joints [1]. In normal joints, the cartilage acts as a cushion and allows the bones to slide and rotate on each other without any type of damage. When OA affects the joint, the cartilage degenerates becoming thinner, and the vanishing of this tissue between the bones causes the reduction of the joint space. The joints start rubbing on each other (see Figure 1.1). This causes an inflammation process, in which the patient suffers intense pain. The bones degenerate by the presence of osteophytes, and the deambulation becomes difficult.

Causes of OA vary from subject to subject. Some people are genetically involved with this pathology, either because they lack a correct production of collagen or because of slight defects in the way the bones are linked together. A great role in the development of OA is played by

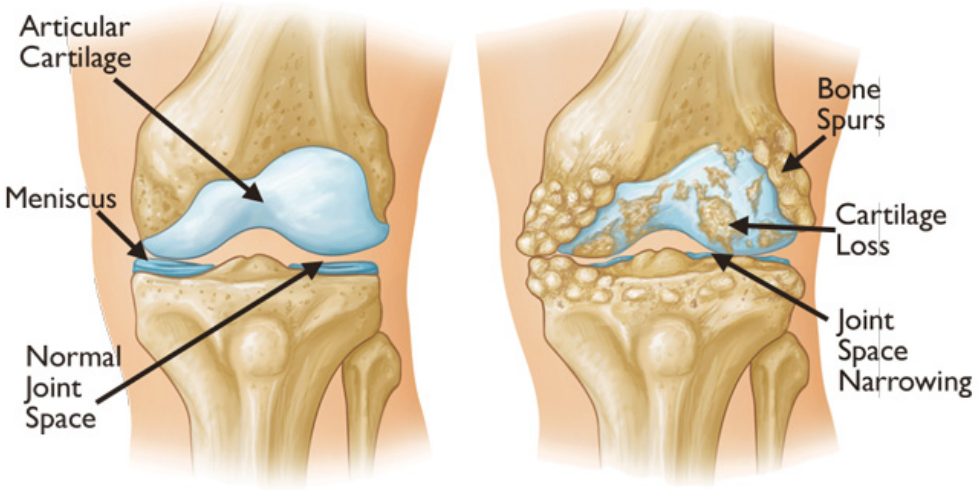

Figure 1.1: *Representation of knee osteoarthritis. Reprinted with permission from OrthoInfo. Â© American Academy of Orthopaedic Surgeons*

the Body Mass Index (BMI) of the subject. Being overweight, in fact, augments the loads that each joint has to carry, in particular in case of knee and hip joint. OA can also be a consequence of injury or overuse of a specific joint. In particular for athletes who repeatedly injure bones or ligaments the cartilage degenerates more quickly, leading to OA. However, the greatest influence on the development of OA is given by ageing. In fact approximately one on every two subjects will develop knee OA in their lives.

The primary treatment for osteoarthritis is conservative. Since the BMI of the subject is important to keep low loads on the joints, the patient is advised to reduce his weight and improve the mobility of the joint. The cartilage benefits from stretching and compression of the joint, especially without weight. The second step involves the reduction of the symptoms with a pharmacological approach. The treatment with analgesics and other anti-inflammatory medicines can be general (with pills and syrup) or local, using creams or lotions that have to be applied directly on the affected joint. The last choice in terms of OA treatment is surgery. The most common surgery is Total Knee Arthroplasty (TKA). The joint is completely removed, and two or three prosthetic components are inserted in the bones, depending on the cases (see Figure 1.2). If the bone is mainly damaged only in one section, the surgeon can decide to

perform osteotomy, avoiding the insertion of prostheses in the knee and restoring the correct load distribution over the surfaces.

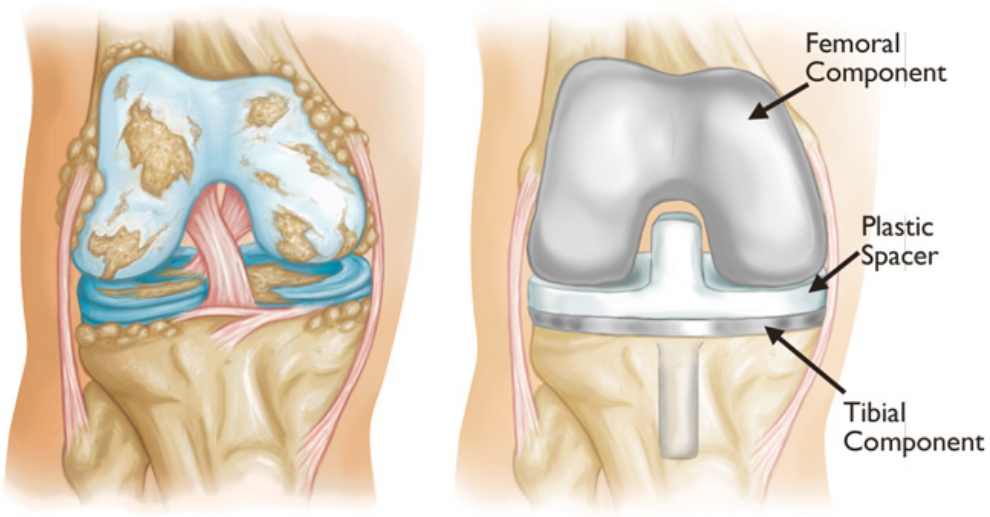

Figure 1.2: *Knee implant representation. Reprinted with permission from OrthoInfo. Â© American Academy of Orthopaedic Surgeons*

1.2 Surgery planning

If the OA grade is very high and there is no other solution, the clinician could decide for surgical intervention. In case of OA, the primary intervention in terms of number of operations is TKA. According to the Organization for economic cooperation and development (OECD) [3], the number of TKA's is increasing from year to year, so that the average number of operations worldwide is doubled from 2000 (ca. 65/100.000) to 2011 (ca. 130/100.000). The increased number of operations per year has opened the way for Computer Assisted Surgery (CAS), that enhances accuracy and repeatability and reduces both time and number of revision needed [51].

The preoperative planning is the main part of CAS and plays a big role in the success of the intervention. Before CAS, surgeons used to have a Computed Tomography (CT) of the patient's knee and one or two whole leg radiographies, that were mainly used to determine the size of the implant and the planning of the resection phase. However, depending on the positioning of the patient during CT scan, the result of the operation could be a little compromised [55]. Errors up to one degree can raise

due to a wrong alignment of the implant during the positioning phase. Current planning software helps the surgeon to decide the size of the implant and check before the operation the direction of the mechanical axis of the knee [36].

The correction of the knee mechanical axis alignment is in fact the major factor of success of TKA. It was found that the same axis can be identified in slightly different directions depending on the operator's ability, on the scan modality and on the difference between standing and lying acquisitions [56]. Inter-operator differences are below one degree, while weight bearing conditions can lead up to three degrees from non-weight-bearing. The differences depends also by the degree of OA that the subject has. In case of a high grade of OA, the weight is decentered and the laxity of the soft tissues determine a different direction of the mechanical axis. This condition can be estimated by standing whole-leg radiographies, but the planning is limited by a bidimensional view. In case of Magnetic Resonance Imaging (MRI) or CT, the subject lies on the bed and the weight is not loading on the soft structures of the knee. This type of modalities can give a deep insight in the morphology of the knee, but cannot be used to estimate the correct direction of the mechanical axis. A combined approach, with the extracted morphology of the bone superimposed on the radiography of the knee, is currently used in clinics [36]. Although this approach saves surgical time, trying to anticipate surgeon decisions in the pre-operatory planning, it still requires a great amount of time and manual accuracy to correctly define the pose of the bones. In addition, the costs of both radiography and CT or MRI are greater than those relying only on X-rays.

Several companies have introduced different commercial software and tools to help the surgeon in the planning phase [2, 5, 6]. These software guide the whole procedure of TKA, from planning to navigation and insertion of the prosthetic component. However, these software rely on 2D images, or, when possible, on 3D shapes extracted from CT or MRI. They do not take into consideration the evaluation of the joint kinematic, even if it would be helpful for some kind of operations.

In order to reduce hospitalization costs and provide to the surgeon the possibility to plan the operation in a 3D scenario, many authors have decided to introduce Statistical Shape Model (SSM) in spite of patient-

specific shape [12, 22, 74, 75].

1.3 State of the art

As described in the previous sections, for a given set of pathologies it is important to have a weight bearing evaluation of the pose of the knee, in order to properly evaluate the effective distance between the bones. In some cases, however, it is also important to evaluate the kinematics of the knee, as a different distance can occur in only some specific poses. Pathological tension of tendons and ligaments, that vary during knee flexion-extension, could be the outcome of a varus or valgus joint, and can cause pain to the patient. The evaluation of the active knee kinematics allows the detection of such tension and the planning of the dedicated intervention.

The preferred method to investigate the kinematics of the knee using a non invasive approach is based on fluoroscopy [8, 12, 62]. The subject is asked to flex the knee while two or more fluoroscopic systems image the interested area. The reconstruction of the movement is done using a patient specific shape segmented from CT or MRI. For each frame, a semi-automatic software enables the superimposition of the shape on the image and the correct detection of the pose.

The most accurate way to determine the pose of the femur during flexion-extension of the knee is using implanted tantalum markers, that are highly visible in the X-rays projections (Figure 1.3) [62, 63]. Radio Stereometric Analysis (RSA) is then used to recover the pose of the beads in the 3D space. However, this approach has two major drawbacks: there must be at least two fluoroscopes to define the size of the shape against the out-of-plane distance and the markers have to be surgically implanted in the bone to be linked to the rigid body, making the procedure highly invasive and not usable in clinics.

The second solution is given by intensity based methods [9, 34, 65]. Those methods are based on a previous CT scan of the joint in order to acquire the density of the bones. The patient-specific bone model is then projected on the image plane integrating the density of each voxel of the CT along the direction of each ray. The synthesized image is then compared to the acquired fluoroscopy and the pose is adjusted until the

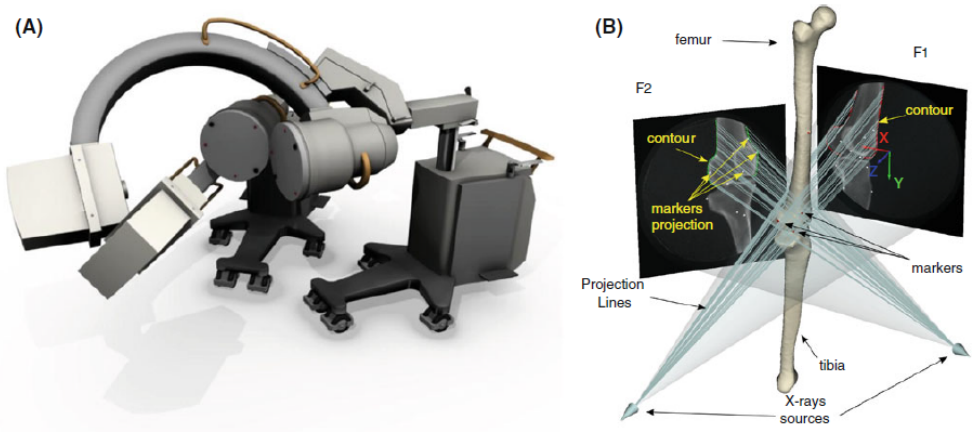

Figure 1.3: *Rendering of a biplanar acquisition setup (a) and virtual representation of the system(b): the implanted markers are used for RSA. Figure extracted from [63]*

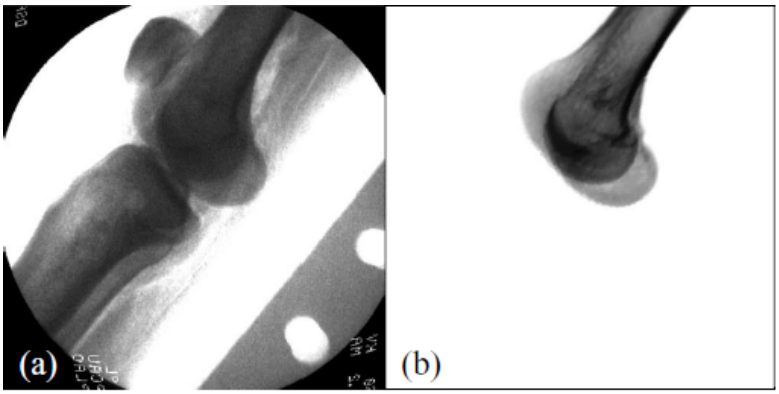

Figure 1.4: *Comparison between a fluoroscopic image of the knee (a) and a Digitally Reconstructed Radiograph of the same femur (b). Figure extracted from [65]*

two images are identical (Figure 1.4).

The third way is feature based methods. Those methods are based on features that are recognizable in the images, such as the contours of the objects. To relate the extracted contour to the 3D shape, the silhouette is selected and projected on the image, and various association functions have been described in literature.

Since feature based methods do not rely on a patient-specific parameters, such as bone density and absorption distribution, a feature based algorithm could be traced out using both subject-specific shapes as CT or MRI, or even a SSM [12, 74]. Those methods, although similar to the previous ones, have the peculiarity to use SSM instead of CT extracted shapes. The morphological scan is avoided, reducing costs and radiation

doses to the patient.

1.4 Aim of the work and thesis structure

Aim of this work is the development of a robust and accurate method for 2D/3D registration of femur shapes on a set of fluoroscopies acquired during knee flexion. The three-dimensional representation of the knee motion allows the complete visualization of each bone segment and their relative motion. Starting from a simple fluoroscopic set of images, the complete motion can be represented, in order to properly perform the pre-operatory planning. Patient-specific models are no more required, as the SSM deformation allows the approximation of the real shape through parameter adaptation. A rough manual initialization is enough to ensure accurate pose registration, and the time required for the surgeon to perform the whole planning is substantially reduced. A graphical user interface helps the surgeon to initialize the algorithm and choose the correct threshold for a canny edge detector in order to select all the contours and avoid as much noise as possible. The same interface offers the surgeon a direct visualization of the 3D model according to the acquired images.

The thesis is organized as follows (see Figure 1.5): in chapter 2 we describe a new method for the construction of the SSM, in chapter 3 we introduced the first method, based on nearest neighbour correspondence and Genetic Algorithm (GA) optimization, while in chapter 4 we described a new method based on Gaussian Mixture Model (GMM) and Maximum Likelihood (ML) estimation. The last chapter contains the conclusion of our work and the results obtained during this three years of research.

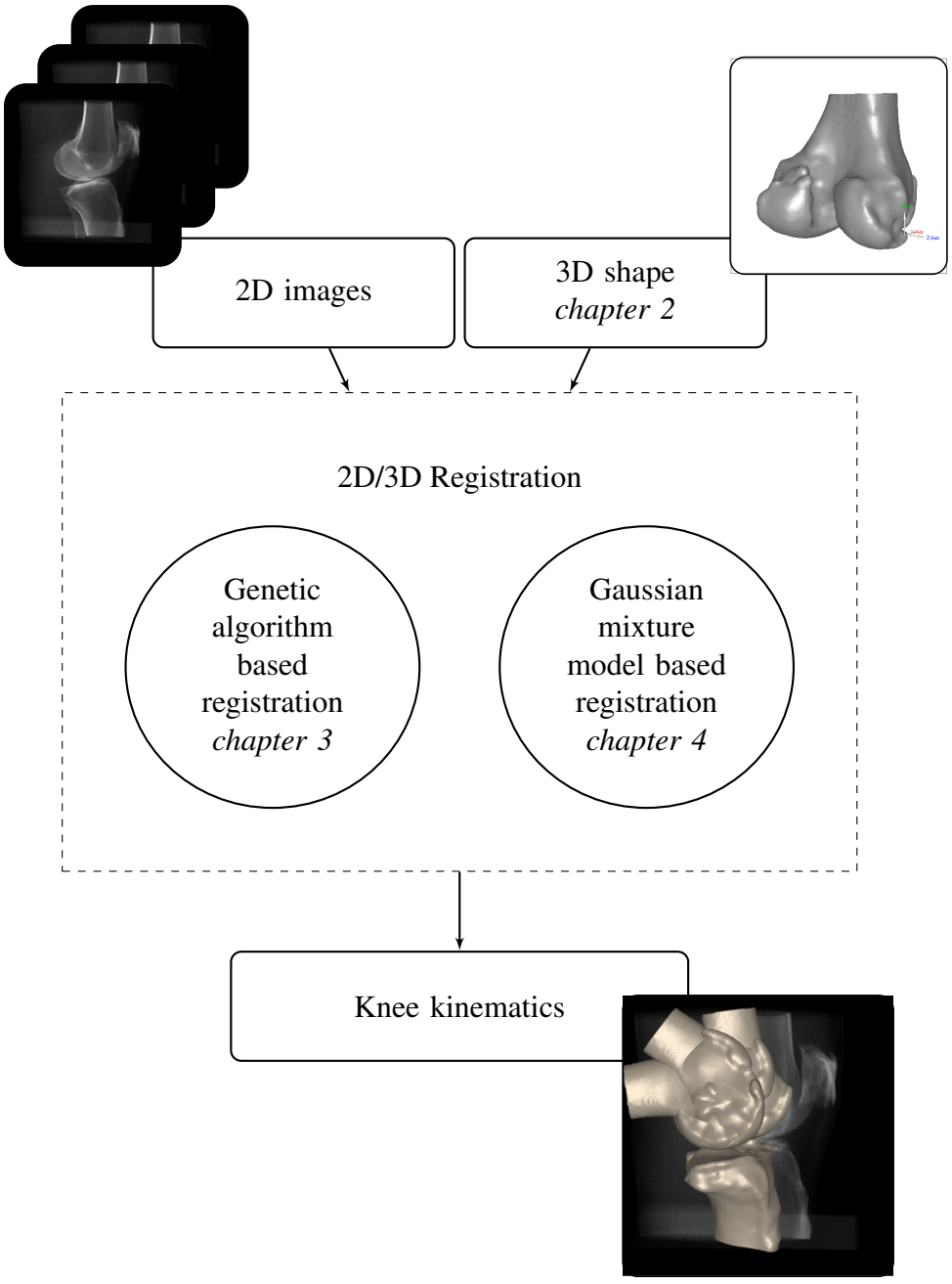

Figure 1.5: *Structure of the thesis*

CHAPTER 2

Statistical Shape Model creation

This work was presented at the MEDICON conference, 2013, with the title *"3D Shape Landmark Correspondence by Minimum Description Length and Local Linear Regularization"* [66].

2.1 Introduction

In the field of computer vision and medical image processing, statistical shape analysis [26] is an important research tool. It offers the possibility to create different models using a set of similar instances of the same object. A Statistical Shape Model (SSM) is a collection of similar shapes, called instances, from which a mean shape is extracted. The covariance of the model is used to deform the shape, according to the principal axis of variation, and the balance between the eigenvectors that deform the model is achieved using different weights [22]. Different types of SSMs have been proposed, allowing accurate modelling of shape structure and variation. Most SSMs treat a shape instance as a vector which is built from landmarks. Therefore, to make different shape vectors comparable and to construct a meaningful SSM, it is crucial that the landmarks identified on different shape instances correspond well (Figure 2.1).

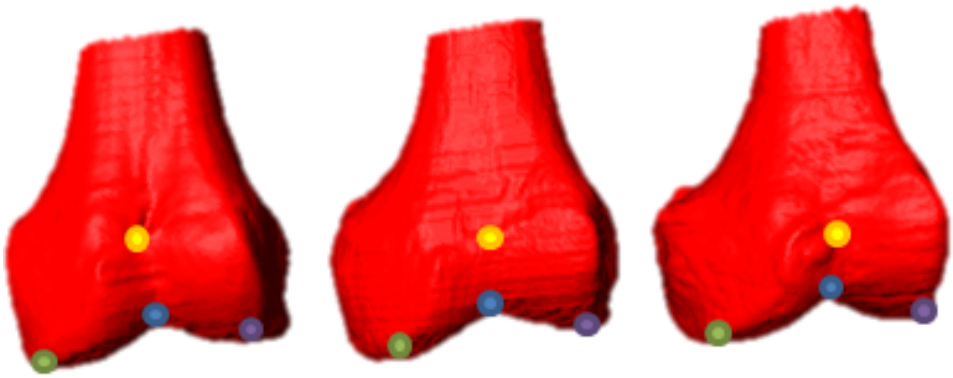

Figure 2.1: *The landmarks are corresponding points on different shapes*

There has been a considerable work on automatic landmark correspondence in literature. An earlier work of Brett and Taylor [18] tackled this problem by ICP algorithm. In [69], the landmark sliding algorithm was proposed which features an objective function which encodes both global shape deformation and local shape topology. However, their algorithm is developed for the construction of 2D shapes, and the iterative structure adopted makes the algorithm itself very slow. Xie and Heng [70] developed an algorithm where the shape correspondence is first established by the shape skeleton features and then refined via point matching by a assignment problem.

Recently, methods based on Minimum Description Length (MDL) criterion have shown promising results. The MDL criterion was first employed for landmark correspondence in [30], and was shown to generate superior results in [59]. In [39], Heimann et al. proposed a new procedure based on the MDL criterion which is less computationally expensive and easier to implement.

In this chapter, we propose a new extension to the existing landmark corresponding method. Our method is based on the framework proposed by [39]. Motivated by the fact that MDL criterion pays more attention on *global* consistency, we introduce a new constraint that enforces the *local* shape similarity. Our new constraint, which is based on the local linear regularization, enforces that the local shape geometry is similar on the corresponding landmark on different shapes. By combining the standard MDL criterion with our new constraint, we end up with an objective

function which enforces the correspondence from both global and local points of view.

We tested our new algorithm using 24 MRI images of pathological knees, entailing femur, patella and tibia. We use the bipartite matching difference and the Wald-Wolfowitz test [54] as performance measures. Our method resulted in a slightly slower algorithm, but comparing our result with the original MDL method we observed an improvement in the case of constructing femur and patella SSMs.

2.2 The Proposed Method

2.2.1 Problem Formulation

Considering a set of M training shapes, each of which is a triangulated mesh $\{S_m = (V_m, E_m)\}$ with $m = 1, \ldots, M$, V_m and E_m are the sets of vertices and edges of the mth training shape (Figure 2.1).

The algorithm as presented by Heimann [39] is based on a spherical parametrization of the shapes. In order to perform this parametrization, all the shapes must be a Genus Zero Surface, a closed surface on which no closed lines can be drawn without disconnecting the surface. We can assure this requirement by closing all the shapes in correspondence of the femoral and tibial cut. Let us denote $\Omega_m(S_m)$ as the spherical parametrization of the mth training shape [64]. For any vertex $v \in V_m$, $\Omega_m(v) \in \mathbb{R}^3$, where $|\Omega_m(v)| = 1$, specify the coordinate of v on the unit sphere (see Figure 2.2).

A set of N landmarks, $\{(\tilde{\theta}_n, \tilde{\phi}_n)\}, n = 1, \ldots, N$ is also defined on the sphere, where $(\tilde{\theta}_n, \tilde{\phi}_n)$ are the spherical coordinates of the nth landmark. To calculate the actual position of the nth landmark on the mth training shape, we build a ray from the origin to $(\tilde{\theta}_n, \tilde{\phi}_n)$ on the parametrization sphere, and calculate the intersection of the ray with the mth shape mesh. We denote a_m^n as the position of the nth landmark on the mth training shape. a_m^n is a vector in the 3D space, that will be a vertex of the reparametrized shape but not necessarily coincident with a vertex of the original shape.

Our goal is to establish landmark correspondence over the training shapes. The landmarks are defined on the parametrization sphere (i.e. $\{(\tilde{\theta}_n, \tilde{\phi}_n)\}, n = 1, \ldots, N$ is fixed for all shapes). For every training

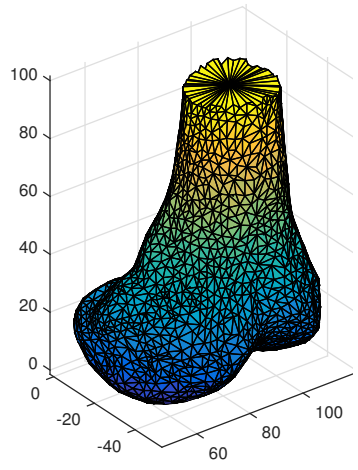

(a) *Original shape S_m*

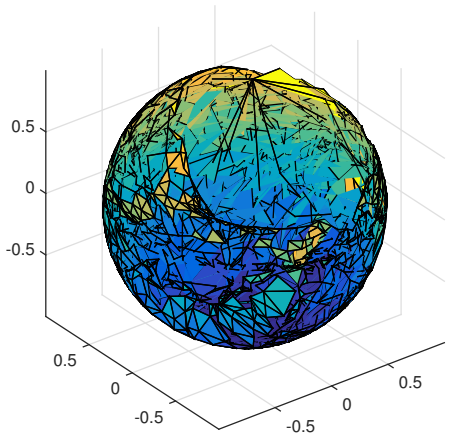

(b) *Initial spherical parametrization Ω_m*

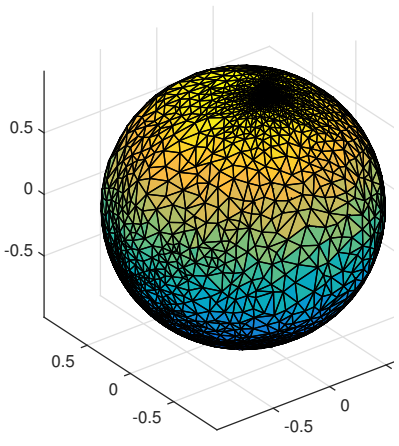

(c) *Resulting spherical parametrization*

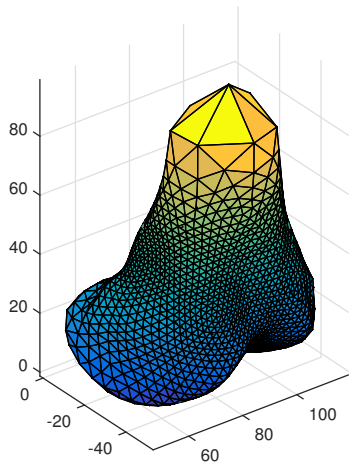

(d) *Parametrized shape*

Figure 2.2: *Description of the spherical parametrization. Starting from the original shape (a), we extract the unit normals of each point on the shape and represent them on the unit sphere (b). After the optimization, the parametrization on the sphere is identical for each shape (c) and we can represent the same shape with the landmarks just defined (d).*

shape S_m, its parametrization Ω_m solely determines $\{a_m^n\}, n = 1, \ldots, N$, the actual position of each landmarks on that shape. Therefore, our goal is searching for the optimal parametrizations $\{\Omega_m\}, m = 1, \ldots, M$ under which the landmark positions over the training shapes have optimal correspondence.

2.2.2 Miminum Description Length cost function

Given the set of all landmark positions on all training shapes $\{a_m^n\}, m = 1, \ldots, M, n = 1, \ldots, N$, in [39], the quality of landmark correspondence (F_{MDL}) is defined as:

$$F_{MDL} = \sum_k \mathcal{L}_m, \text{where} \tag{2.1}$$

$$\mathcal{L}_m = \begin{cases} 1 + \log(\lambda_m/\lambda_{cut}), & \text{if } \lambda_m \geq \lambda_{cut} \\ \lambda_m/\lambda_{cut}, & \text{if } \lambda_m < \lambda_{cut} \end{cases} \tag{2.2}$$

where λ_{cut} is a parameter which represents the expected noise in the training data and λ_m is the m^{th} eigenvalue of the distribution, composed by M training shapes. k is the total number of eigenvalues of the model. In [39], the parametrization $\{\Omega_m\}, m = 1, \ldots, M$ is optimized so that the corresponding landmark positions $\{a_m^n\}, m = 1, \ldots, M, n = 1, \ldots, N$ generates the minimum F_{MDL}.

2.2.3 Local Linear Regularization cost function

In this chapter we extend the original MDL-based approach with a new objective function considering the local linear similarity. The idea is to enforce the geometric consistency in the local neighbourhoods of each landmark over different shapes. To do this, we first create a neighbourhood system $\mathcal{N}$ of the landmarks. Specifically, for the nth landmark, $\mathcal{N}(n) = \{\mathcal{N}(n)_k\}, k = 1, \ldots, K_n$ is the set of K_n landmark indices that are within its local neighbourhood. Each neighbour shares with the selected landmark one edge of the landmark shape. Then, considering a_m^n, which is the position of the nth landmark on the mth training shape, it should be reasonably reconstructed using its neighbouring landmarks on the same shape:

$$a_m^n = w_{m,n}^1 a_m^{\mathcal{N}(n)_1} + \cdots + w_{m,n}^{K_n} a_m^{\mathcal{N}(n)_{K_n}} = A_m^n W_{m,n} \tag{2.3}$$

where $A_m^n = \left[a_m^{\mathcal{N}(n)_1}, \ldots, a_m^{\mathcal{N}(n)_{K_n}}\right]$ is the matrix of neighbouring landmarks of a_m^n, and $W_{m,n} = \left[w_{m,n}^1, \ldots, w_{m,n}^{K_n}\right]^\top \in \mathbb{R}^{K_n}$ is the reconstruction coefficient vector. Note that Eq. (2.3) only considers reconstructing a single landmark on a single shape. In a usual non-degenerate case, Eq. (2.3) is underdetermined as long as $K_n > 3$. However, if we consider the nth landmark on *every* training shape, it is natural to require that the same reconstruction weight is used to reconstruct the same landmark on all shapes. That is, $W_{m,n}$ should be independent of m. We thus drop the subscript m, and denote the reconstruction weight as W_n, and Eq. (2.3) becomes a system of equations defined on all shapes:

$$\forall m = 1, \ldots, M : a_m^n \approx A_m^n W_n \tag{2.4}$$

Note that since in our case the number of training shapes is larger than the number of neighbours, Eq. (2.4) becomes overdetermined and W_n can be solved by Least Mean Squares (LMS) method, given that the landmark positions a_m^n and A_m^n are known. In this way we can compute $\{W_n\}$ for $n = 1, \ldots, N$, and then the quality of landmark correspondence (F_{LLR}) can be expressed as the summation of reconstruction errors of all landmarks over all shapes:

$$F_{LLR} = \sum_{n=1}^{N} \sum_{m=1}^{M} \left\| a_m^n - A_m^n W_n \right\|^2 \tag{2.5}$$

Eq.(2.5) is our objective in terms of the local linear regularization. We add it to the original objective based on MDL, and get the final objective function (F):

$$F = F_{MDL} + \alpha F_{LLR} \tag{2.6}$$

with $\alpha \in [0, 1]$ being a positive weighing parameter controlling the relative importance of the new term.

2.2.4 Optimization Process

To find the parametrizations $\{\Omega_m\}$ that optimize the objective function, we adopt a similar optimization strategy as in [39] and adapt it to our objective function with the new term.

Initialization For each training shape S_m, we initialize Ω_m as a conformal parametrization as in [64].

Iterative Optimization We iteratively optimize the set of parametrizations $\{\Omega_m\}$. In each iteration, for each shape, we locally update the parametrization using an update function $\Omega' = \Phi(\Omega)$ which is parametrized as $\Omega' = \Phi_{c,\sigma,\Delta\theta,\Delta\phi}(\Omega)$, where c and σ are the centre and bandwidth of the update kernel, and $\Delta\theta$ and $\Delta\phi$ specify the update direction. We use a Gaussian envelope kernel:

$$\rho(x) = \begin{cases} \exp\left(\frac{-\|x-c\|^2}{2\sigma^2}\right) - \exp\left(\frac{-(3\sigma)^2}{2\sigma^2}\right) & \text{for } \|x-c\| < 3\sigma \\ 0 & \text{for } \|x-c\| \geq 3\sigma \end{cases} \tag{2.7}$$

Eq. (2.7) gives the magnitude of change at any point x on the mesh. Combined with the direction of update, we actually change the spherical coordinate of x by $\rho(x) \cdot (\Delta\theta, \Delta\phi)$.

During the optimization, three different kernel configurations are used, with σ decreasing to optimize larger regions at the beginning and details at the end. The centers of the kernels are coded in order to avoid errors due to the presence of a pole. In this case, the vertices would all move towards or away from this point, resulting in a degenerated parametrization.

The update direction $(\Delta\theta, \Delta\phi)$ in each iteration is determined through the gradient of the objective function with regard to $(\Delta\theta, \Delta\phi)$. Since the influence of $(\Delta\theta, \Delta\phi)$ to the objective F is via the landmark positions we have:

$$\frac{\partial F}{\partial(\Delta\theta, \Delta\phi)} = \frac{\partial F}{\partial a_i^j}\frac{\partial a_i^j}{\partial(\Delta\theta, \Delta\phi)} \tag{2.8}$$

where $\frac{\partial a_i^j}{\partial(\Delta\theta,\Delta\phi)}$ is calculated by finite difference method. $\frac{\partial F}{\partial a_i^j}$ is calculated analytically. From Eq. (2.6), we have:

$$\frac{\partial F}{\partial a_i^j} = \frac{\partial F_{MDL}}{\partial a_i^j} + \alpha\frac{\partial F_{LLR}}{\partial a_i^j} \tag{2.9}$$

where $\frac{\partial F_{MDL}}{\partial a_i^j}$ is calculated as in [39]. For $\frac{\partial F_{LLR}}{\partial a_i^j}$, note from Eq.(2.5) that in each component of summation $\|a_m^n - A_m^n W_n\|^2$, depending on the relation of (m, n) and (i, j), a_i^j might not appear, or might appear in a_m^n or A_m^n (but not both). Therefore:

$$\frac{\partial F_{LLR}}{\partial a_i^j} = \sum_{m=1}^{M}\sum_{n=1}^{N} f'_{(m,n)}(i,j), \quad \text{where} \tag{2.10}$$

$$f'_{(m,n)}(i,j) = \begin{cases} 2a_i^j - 2W_j A_i^j & \text{if } (m,n) = (i,j) \\ 2W_n^d(W_n A_i^n - a_i^n) & \text{if } m = i \text{ and } j = \mathcal{N}(n)_d \\ 0 & \text{otherwise} \end{cases} \tag{2.11}$$

2.3 Experiments

In order to evaluate the performances of our new method, we used a dataset of 24 MRI images of pathological knees. The images were manually segmented using Amira® (VSG3D, France), then reduced and rigidly aligned. We then used both methods to register three different groups of anatomical structures, namely femurs, patellas and tibias. Table 2.1 shows the number of points of each mesh and the number of landmarks used for each group.

Table 2.1: *Schema of the three different experiments done*

Group	Anatomical part	# points	# landmarks
1	Femur	5002	2562
2	Patella	5002	642
3	Tibia	5002	2562

For each group, we ran the algorithm with α equal to 0 (for the original algorithm) and with $\alpha = 0.5$ representing our new implementation (cfr. Eq.(2.6)). To evaluate the performance of the two algorithms we used the coefficient described in [54]. This paper states that the well known measurements of compactness, specificity and generalization could have some limitation in the evaluation of a statistical shape model. In [54] Munsell et al. describe a new benchmark for the evaluation of 2D shape-space based on a given ground truth. We extended this method to 3D volume-space, and used the original shapes as ground truth. Formally, the evaluation of the shape correspondence follows these steps:

- each shape resulting from the two algorithms ($\{S_i^r\}_{i=1}^M$) is rigidly realigned with its original shape ($\{S_i^o\}_{i=1}^M$), in order to reduce errors due to misalignment of the two datasets.

- each shape, including the ground-truth shapes, is then voxelized with a grid of $0.5 \times 0.5 \times 0.5$ mm.

Rigid re-alignment does not change the position of the landmarks with respect to the object reference frame, but a common reference frame is needed for all the shapes in order to compare the two volumes. At this point we need to introduce the Jaccard coefficient. This is defined as

$$\Delta(S_1, S_2) = 1 - \frac{|R(S_1) \cap R(S_2)|}{|R(S_1) \cup R(S_2)|} \tag{2.12}$$

where S_1, S_2 are the two shapes considered and $|R|$ computes the volume enclosed in the surface.

2.3.1 Bipartite matching difference measure

The first measure we define is based on the bipartite-matching difference between $\{S_i^o\}_{i=1}^M$ and $\{S_j^r\}_{j=1}^M$. We build up the graph that has $2M$ vertices for the shapes $\{S_i^o\}_{i=1}^M$ and $\{S_j^r\}_{j=1}^M$. The weight of the link between two different shapes is given by the Jaccard coefficient between the two shapes linked. Then, applying the bipartite matching algorithm (with the Hungarian method [46]), we can match each ground truth shape with each result shape in order to minimize the sum of the weights. The bipartite matching difference measure is defined as

$$\Delta_b = \frac{\sum_{i=1}^M \Delta\left(S_i^o, S_{b(i)}^r\right)}{M} \tag{2.13}$$

where $\Delta\left(S_i^o, S_{b(i)}^r\right)$ is the Jaccard difference of the identified corresponding shapes. Thanks to the normalization, Δ_b is always a value in $[0, 1]$; $\Delta_b = 0$ implies that the two shape space compared come from the same distribution, while if $\Delta_b = 1$ they describe two completely different shape spaces.

2.3.2 Wald-Wolfowitz test

The bipartite matching difference compares couples of two corresponding shapes individually and returns the mean difference between the two populations. However, even if this measure is equal to 0 (indicating that the two shapes are identical), it could be that the two populations that generated the samples are different. To overcome this limitation, we introduced another measure, as in [54]. The second measure we take into consideration is the Wald-Wolfowitz generalized test, based on the minimum spanning tree (MST) algorithm. For this algorithm, we build a fully connected undirected graph with 2M vertices, that represent both $\{S_i^o\}_{i=1}^M$ and $\{S_i^r\}_{i=1}^M$. Then we define the weight of each edge connecting two shapes (both inter and intra the two spaces) as the Jaccard coefficient between the two shapes. We then find the MST of the constructed graph, that is the spanning tree with the minimum total edge weight. On this tree, we count the number of edges that connect two shapes from the same space, either inside $\{S_i^o\}_{i=1}^M$ or $\{S_i^r\}_{i=1}^M$. We can call this number W. Normalizing W over $2M - 2$ we finally get the Wald-Wolfowitz difference measure (Δ_w).

The Δ_w value is thus always included in $[0, 1]$. In particular, a smaller value of Δ_w indicates that the two distributions most likely come from the same shape space.

2.3.3 Results

We evaluate the performances of the two algorithms both with the two methods described above and with a visual/qualitative comparison.

Qualitative differences between the two models are highlighted in Figure 2.3 and 2.4. For the quantitative results, Table 2.2 describes the two index achieved with $\alpha = 0$ (as in [39]) and $\alpha = 0.5$ (the present algorithm) for the investigated bones.

2.3.4 Discussion

Quantitative results show that our method performs better in case of femur and patella, while no improvement is made in case of tibia. Evaluating visually the performance, we can see that tibia has some sharp contours that cannot be rightly approximated by our algorithm, based

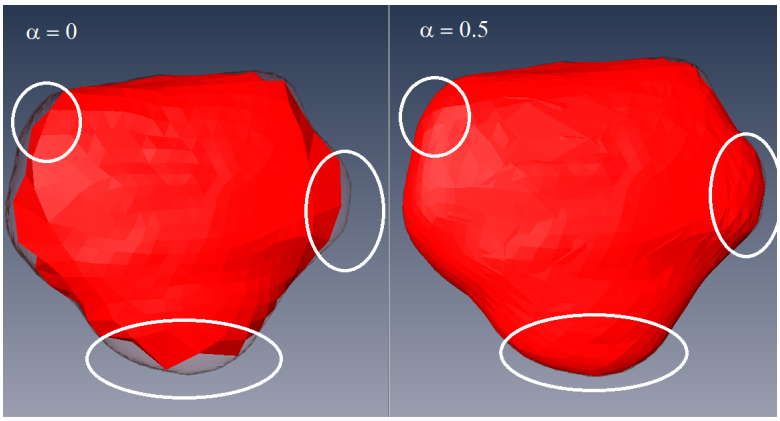

Figure 2.3: *Same patella mesh processed with two different values of* α

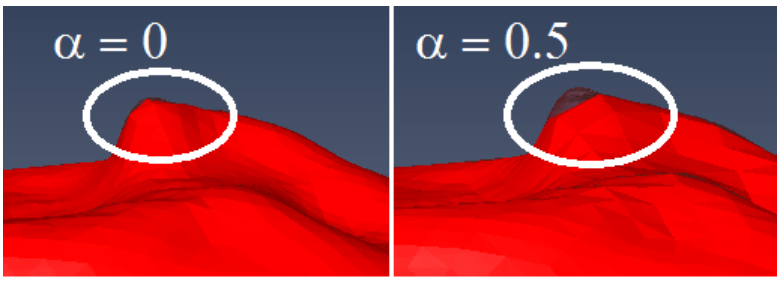

Figure 2.4: *Same tibia mesh processed with two different values of* α

Table 2.2: *Schema of the results achieved*

Anatomical part	index	$\alpha = 0$	$\alpha = 0.5$
Femur	Δ_b	0.0226	0.0204
	Δ_w	0.4348	0.3913
Patella	Δ_b	0.0786	0.0449
	Δ_w	0.500	0.4783
Tibia	Δ_b	0.0108	0.0117
	Δ_w	0.4565	0.500

on the similarity of neighbouring points. However, such low levels of Δ_b achieved for tibia with both algorithms, indicates that the two shape space contain similar meshes and also that a shape has the same probability density in these two shape spaces.

2.4 Conclusions

We describe a new algorithm to improve landmark correspondences on different shapes for statistical shape analysis. We evaluate our method with two different quantitative measures and with a qualitative overview of the results.

While our method is better in two cases (femur and patella) out of three, we cannot state that for every shape we can achieve better results. Further investigation will be done on other bones, in order to asses the improvement given by our landmark correspondences optimization method.

CHAPTER 3

Femur kinematics registration based on Genetic Algorithms

This work was presented in the CARS international conference, IPCAI, 2015, with the title *"Fluoroscopy-based tracking of femoral kinematics with statistical shape models"*, and has been accepted for publication in the International Journal of Computer Assisted Radiology and Surgery [67].

3.1 State of the art

Knee kinematics assessment has great importance both to understand the problems associated with a large number of knee pathologies and to improve the design of prosthetic components [11, 12]. In case of severe osteoarthritis, that are eligible for joint implant surgery, in vivo pre-operatory knee kinematics is fundamental to understand the relative motion between the three joint bones. The relative movement can give an insight of how the ligaments are stretched and their stability, and how could be the feeling for the patient. In this way, pre-operatory knee kinematics could help the surgeon to decide which prosthesis should be used and how to correct the misalignment of the bones [8].

Table 3.1: *Pros and Cons of the different methods to acquire knee kinematics*

Method	Pros	Cons
Skin mounted markers and external cameras	Non invasive	Motion artefacts
Implanted markers and x-ray projector	Very accurate	Highly invasive
Fluoroscopy with CT or MRI shape	Mostly accurate	Highly expensive
Fluoroscopy with SSM	Non invasive, cheap	Accuracy depends on the deformation ability of the model

Currently, the reconstruction of the pose of the knee can be done using 3D scan such as real time Magnetic Resonance Imaging (MRI) or through a 2D/3D registration method that superimposes the shape extracted from MRI or Computed Tomography (CT) onto an image, usually X-ray or fluoroscopy. Real-time MRI is suitable to study joint kinematics, as it evidences the muscle structure during movements. However, it can only be used with relatively slow movements, and the accuracy obtained increases from 1 mm to more than 3 mm depending on the velocity of the movement. In addition, MRI scans are highly expensive [35]. Traditional CT and MRI provide an accurate evaluation of the morphology of the knee, but are limited to static positioning of the patient. A great number of pathologies, such as patellofemoral pain and osteoarthritis require a dynamic evaluation of the knee motion [8, 12, 62].

Four main methods are used in research centers to in-vivo assess knee kinematics (see Table 3.1): using skin-mounted markers, implanted markers and 2D image based methods both with patient specific shapes or with Statistical Shape Model (SSM).

Skin-mounted retro-reflective markers are used in gait analysis [20, 42, 47] using optical localization techniques. Since this type of measurement suffers from relative motion between the skin and the bone, results are not reliable to properly investigate joint kinematics.

The second method is based on tantalum markers implanted in the bone; even if this method is much more precise than the previous one, it is not commonly used in clinics due to the high invasiveness of the intervention [32, 61, 62]. In [60], the authors used mono and biplane fluoroscopic images to accurately reconstruct the pose of the patella, implanting markers in cadaver specimens and artificially flexing the knee joint.

The use of dynamic fluoroscopy to detect knee kinematics is described in [34].The authors use a fluoroscopic system flashing at 30Hz, obtaining continuous images of the knee flexion from 0° to 120°. A static CT is projected to reconstruct knee kinematics. A similar protocol is used in [7]; the authors describe a method to align CAD projections of knee implants to fluoroscopic images. They perform dynamic acquisitions at 8Hz moving a Sawbone model with an implant between 0° and 90°. In [38], the authors introduced SSMs to reconstruct the shape of the femur. They performed a deep analysis on the optimal number of X-ray scans that allow an accurate reconstruction of the shape of the knee. Their method was based on manual segmentation of the bone contour from X-ray images. In [12], the authors introduced a fully automatic technique to extract the contour from the fluoroscopic images, based on a Canny edge detector [19]. They used two fluoroscopic sequences of drop-landing motion with intra-fluoroscopic distance between $58^\circ - 82^\circ$. They used a cadaveric knee as gold standard, implanting tantalum markers and simulating motion of the knee while doing fluoroscopic imaging of the joint. Their mean errors are less than 1 millimiter, spanning to 4 mm both with the CT-extracted shape and the SSM. However, the method proposed by Baka was only evaluated on healthy subjects, without evidence that the same accuracy could be obtained with osteoarthritic patients.

The aim of this work is to solve a registration problem between 2D images and 3D shape using a method based on Genetic Algorithm (GA). We focused our study on the kinematics of the femur, but the algorithm can be easily extended to the whole kinematics of the knee. We used osteoarthritic femurs in order to expand the validity of the method not only to healthy subjects. The SSM created in the previous chapter (2) was used in this chapter to register the pose of the femur on fluoroscopic

images acquired during knee flexion-extension. The method was evaluated generating Digitally Reconstructed Radiographs (DRRs) from static CT acquisitions of osteoarthritic patients and simulating femur flexion-extensions. We evaluate the accuracy of the pose reconstruction of the distal femur both with the CT segmented shape and SSM. We expect an accuracy index lower than the one found by Baka et al. [13], as we are introducing deformities due to osteoarthritis. However, with the CT segmented shape the results should be comparable, as the shape is not deformed.

3.2 Methods

Our femoral kinematics tracking method is based on SSM which pose is obtained using a biplane fluoroscopy. We applied a GA optimization technique, in order to improve the accuracy (Figure 3.1).

The tracking algorithm is divided into three main phases:

- Statistical Shape Model creation (3.2.1)
- Shape pose initialization (3.2.2)
- Femur tracking (3.2.3)

3.2.1 Statistical Shape Model (SSM) creation

SSM gives an effective parameterization of the shape variations found in a collection of sample models of a given population [23, 74]. For our study we used the distal part of the femur only. Each bone model ($\mathbf{M}_o$ with $o = 1, \ldots, O$) is represented as an ordered set of $p = 1, \ldots, P$ vertices $\mathbf{M}_o = [x_1, y_1, z_1, \ldots, x_p, y_p, z_p, \ldots, x_P, y_P, z_P]$ and a list of triangular facets connecting the vertices. Applying the algorithm described in chapter 2 [68], we found the correspondence between corresponding vertices on different shapes. The SSM is defined as the mean model $\bar{\mathbf{M}}$ and a set of eigenvectors obtained applying Principal Component Anal-

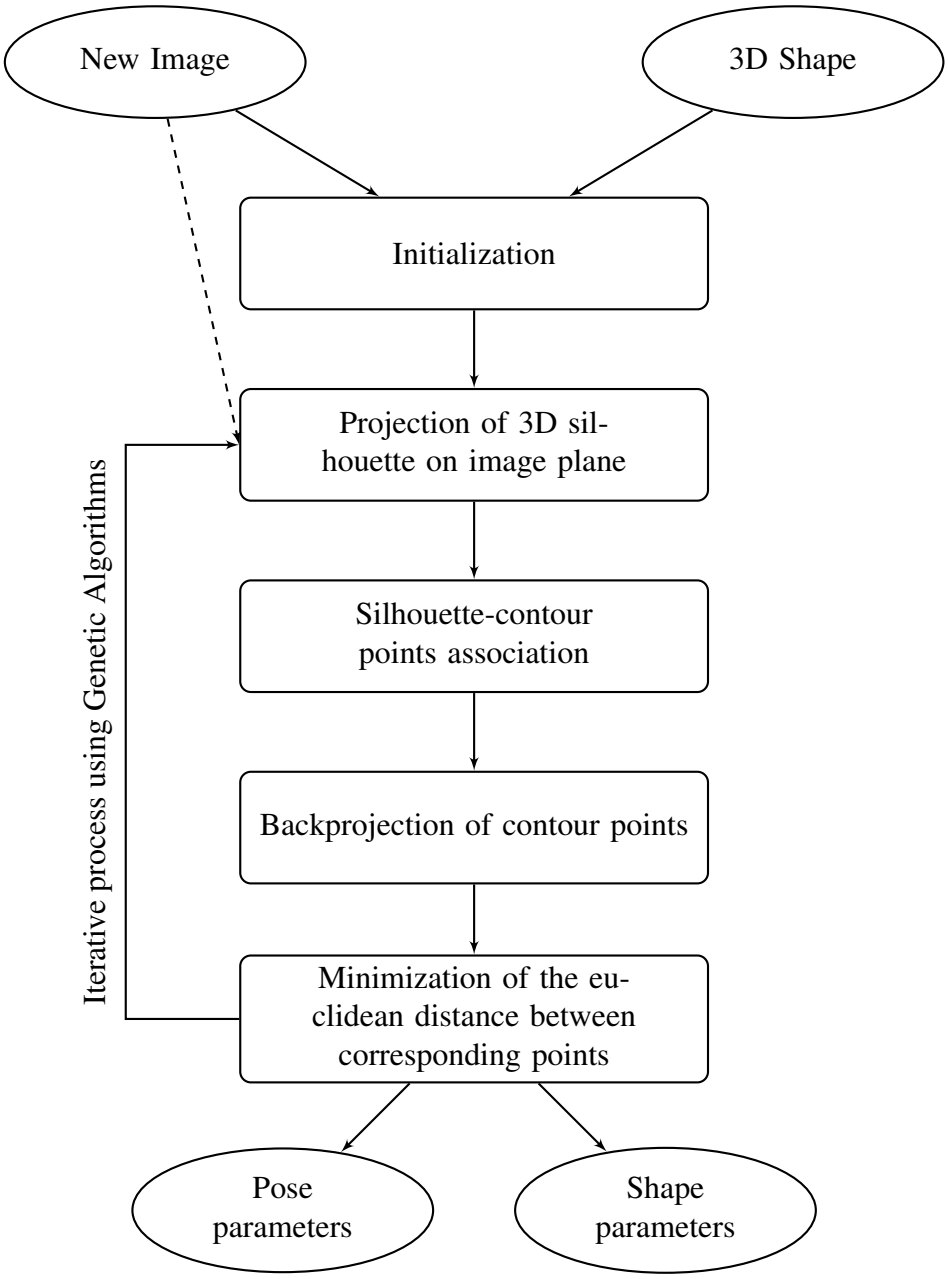

Figure 3.1: *Flowchart of the GA based algorithm.*

isys (PCA) to the model vectors $\mathbf{M}_o$.

$$\begin{aligned} \mathbf{D} &= \frac{1}{O-1}\sum_{o=1}^{O}(\mathbf{M}_o - \bar{\mathbf{M}})(\mathbf{M}_o - \bar{\mathbf{M}})^T \\ \mathbf{D}\cdot\overrightarrow{\mathbf{M}}_o &= \sigma_o^2\cdot\overrightarrow{\mathbf{M}}_o \\ \sigma_1^2 &\geq \sigma_2^2 \geq \cdots \geq \sigma_{O-1}^2 \end{aligned} \tag{3.1}$$

where σ_o^2 are the descending-order eigenvalues of the covariance matrix $\mathbf{D}$ and $\overrightarrow{\mathbf{M}}_o$ are the corresponding eigenvectors. Every instance of this SSM is then expressed as:

$$\mathbf{M}_{SSM} = \bar{\mathbf{M}} + \sum_{o=1}^{O'}\alpha_o\overrightarrow{\mathbf{M}}_o \tag{3.2}$$

where α_o is the weight corresponding to the o^{th} eigenvector $\overrightarrow{\mathbf{M}}_o$ and O' is the number of significant eigenvalues ($O' < O$). In our dataset, $O = 24, O' = 23$. For this study, we used 24 MRI datasets of healthy knees, from which we semi-automatically segmented the femur contours using Amira® (VSG | FEI, Mérignac Cedex, France). From each volume, we extracted the femur's triangulated surface with 2562 points and 5120 facets using the marching cubes technique [50]. To create the SSM, corresponding points on different shapes have to be determined [27] [24]. In our case, corresponding points between the O shapes were selected using the automatic algorithm described in chapter 2 [68]. Within the corresponding models, we computed the mean model and the covariance matrix.

All the patients signed an informed consent and the institutional review board approved the study.

3.2.2 Shape pose initialization

The femur tracking dataset is composed of two fluoroscopic frames acquired during knee flexion-extension at each time step t with $t = 0, \ldots, T$. The contour of the distal femur is extracted on each fluoroscopic image.

We defined a set of $I(I = 7)$ landmarks on the mean model ($\mathcal{L}_{i(\bar{\mathbf{M}})}$, with $i = 1, \ldots, I$) that were used to initialize the pose of the SSM in the world Reference Frame (RF) ^{w}RF (Figure 3.3). The landmarks were

identified as the most identifiable anatomical landmarks in the images. Recent studies have addressed the topic of automatically segment contours from X-Ray images using random forests [25, 48]. However, these methods need to be trained over a consistent number of images to be used with non-standard projections. In order to save time and to give the possibility to use any angle of projection the operator is asked to manually identify the I corresponding landmarks on the two fluoroscopic images at $t = 0$ ($\ell_{i(n)}$ with $i = 1, \ldots, I$ and $n = 1, 2$, where i indicates the number of the landmark and n indicates the view). For each test, the user has to define 7×2 landmarks on the 2 images, based on the highlighted position of the landmark on the 3D SSM. We also tested if the initialization was user-dependent. Our study [68] proved that the algorithm is stable with an initialization error up to 3 cm.

Each fluoroscopic image has its own calibration parameters, so that we know the position of the source and the position of the image plane in the ^{w}RF, as well as its normal vector. The initialization is used to estimate the initial position of the SSM with respect to the 2 fluoroscopic images, i.e. ${}^{w}\mathbf{T}_{m}^{0}$. We can back-project each landmark pixel ($\ell_{i(n)}$) to the corresponding source $\mathbb{S}_n$. In this way, for each landmark we find 2 skew lines (one for each projection) that should (ideally) intersect in one point (the 3D position of the landmark) but, due to errors and noise, they actually do not intersect. Thus to define the position of the landmark we take the middle point of the shortest line connecting the rays (see Figure 3.2).

As the landmarks are defined both in the 3D space and on the model, we can use a simple registration algorithm for corresponding points to find the initial pose of the model in the 3D space [58]. $\mathcal{L}_{i(\bar{\mathbf{M}})}$ is the landmark on the model surface, the similarity transformation ${}^{\mathbf{w}}\hat{\mathbf{T}}_{\mathbf{m}}^{\mathbf{0}}$ (rotation $\mathbf{R}$, translation $\mathbf{t}$ and scaling factor s) transforms the model landmarks into $\mathcal{L}_{i(SSM)}$ (Figure 3.3). To obtain the transformation ${}^{\mathbf{w}}\hat{\mathbf{T}}_{\mathbf{m}}^{\mathbf{0}}$ we define a cost function F based on the Euclidean distance between the transformed landmarks and the position of the points defined by the backprojection

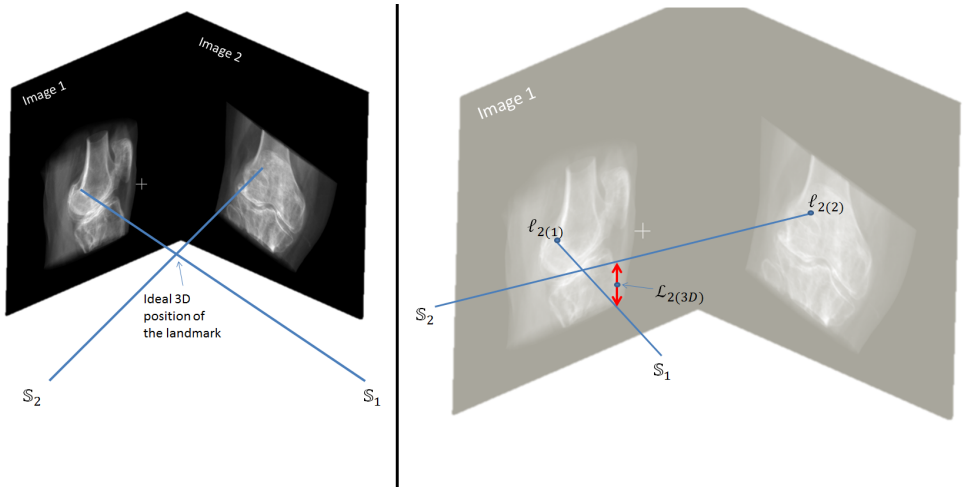

Figure 3.2: *Definition of the landmark pose in the 3D space. In the right part of the figure the position of the real landmark is shown ($\mathcal{L}_{i(3D)}$*

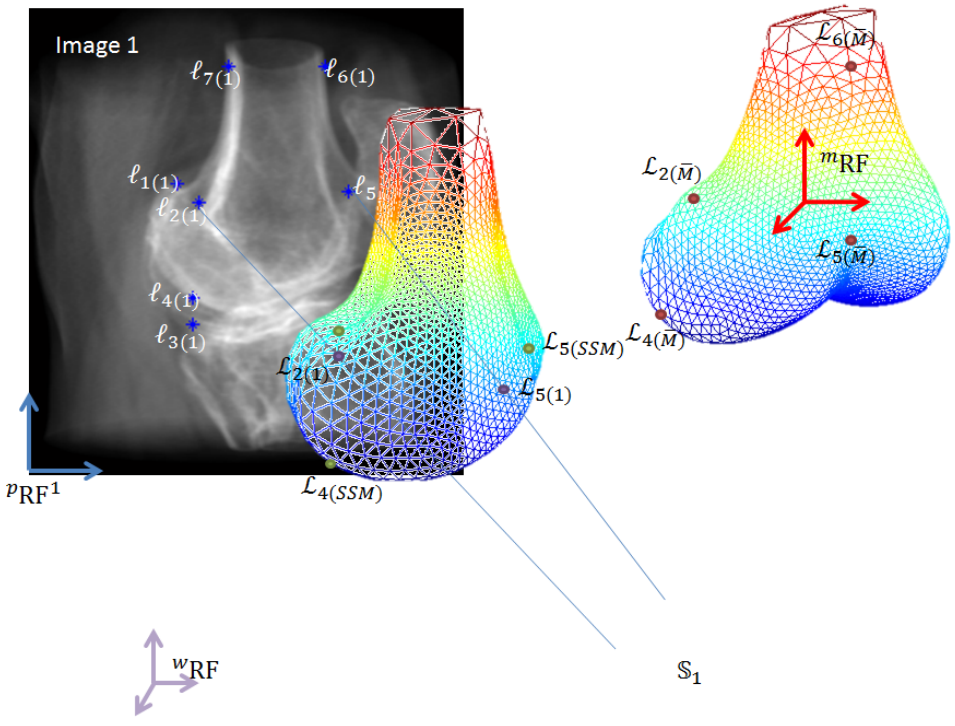

Figure 3.3: *Schematic of the reference frames involved in this algorithm. Points on the image plane, expressed in pixel index (i, j), are in the $^{p}RF^{n}$, where n indicates the number of the image plane. ^{m}RF is the reference frame of the SSM, and ^{w}RF is the world reference frame. Points in red on the model are the landmarks $\mathcal{L}_{i(\bar{M})}$, points in blue on the image are the selected landmarks on the first image $\ell_{i(n)}$, points in purple are the landmarks in the ^{w}RF extracted from source-image rays ($\mathcal{L}_{i(n)}$) and points in green are the model landmarks in the ^{w}RF after the initialization ($\mathcal{L}_{i(SSM)}$).*

of the landmarks on the images $\mathcal{L}_{i(3D)}$.

$$\begin{aligned} F &= \sum_{i=1}^{7} ||\mathcal{L}_{i(3D)} - \mathcal{L}_{i(SSM)}|| \\ \mathcal{L}_{i(SSM)} &= s \cdot \mathbf{R} \cdot \mathcal{L}_{i(\bar{\mathbf{M}})} + \mathbf{t} \end{aligned} \tag{3.3}$$

We thus apply the same transformation matrix ${}^{\mathbf{w}}\hat{\mathbf{T}}^{\mathbf{0}}_{\mathbf{m}}$ to all the points of the mean model ($\bar{\mathbf{M}}$).

$$\mathbf{M}_{(SSM)} = {}^{\mathbf{w}}\hat{\mathbf{T}}^{\mathbf{0}}_{\mathbf{m}} \cdot \bar{\mathbf{M}} \tag{3.4}$$

3.2.3 Femur tracking

After the manual initialization of the pose in the first frames, the algorithm returns the pose of the shape as homogeneous matrix ${}^{w}\mathbf{T}^{t}_{m}$. To track the pose of the femur in the ^{w}RF during time, we repeat the following *Pose optimization* steps for each sample time $t = 0, \ldots, T$. In each frame the initialization is given by the homogeneous matrix of the previous frame (${}^{w}\mathbf{T}^{t-1}_{m}$).

The shape of the femur is optimized at $t = 0$, as described in the *Shape optimization* paragraph, and then kept constant for all the tracking times.

Pose optimization

Using the initialization of the SSM's pose in the ^{w}RF, for each given image plane ${}^{i}\text{RF}^{n}$ we can extract the silhouette of the model, identifying the points that share a "contour" edge. This edge is in common between two facets that have the normals pointing in opposite directions from the corresponding source $\mathbb{S}_{(n)}$(see Figure 3.4). We define the silhouette of the model as $\mathbf{S}_{j_n(n)}$, with $j_n = 1, \ldots, J_n; n = 1, 2$, where each point is shared between two "contour" edges. We then project the silhouette extracted on the corresponding image plane, defining the corresponding set of pixels on each image plane as $\mathbf{s}_{j_n(n)}$.

For each contour pixel in $\mathbf{c}_{k_n(n)}$ we find the nearest pixel of $\mathbf{s}_{j_n(n)}$, and associate it to the corresponding silhouette point in $\mathbf{S}_{j_n(n)}$. We call $\mathbf{S}_{k_n(n)}$ the associated silhouette point.

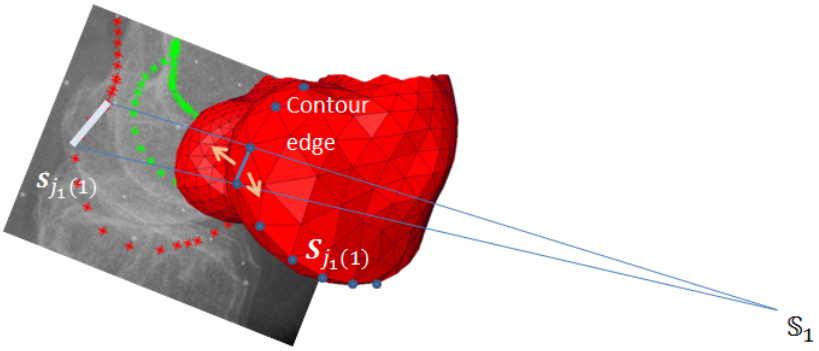

Figure 3.4: *Definition of the contour edge describing the silhouette of the model. The red points are the projection of the silhouette points. The green points are the extracted contour.*

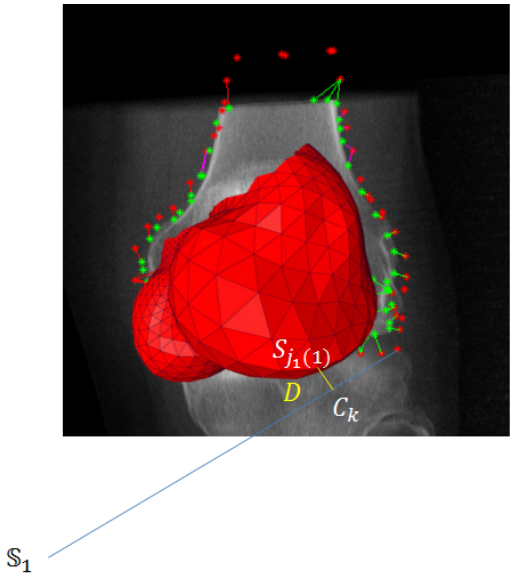

Figure 3.5: *Definition of the objective function: minimization of the distance D*

For each point on the image plane we define the projection line from the source ($\mathbb{S}_{(n)}$) and find $\mathbf{C}_{k_n(n)}$, the closest point on the line between the line and the corresponding silhouette point $\mathbf{S}_{k_n(n)}$, as shown in Figure 3.5.

The cost function $F_{pose}$to minimize can thus be defined as:

$$
\begin{aligned}
F_{pose} &= \min_{{}^{w}\mathbf{T}_m^t} \left(\sum_{k_n=1}^{K_n} D_{k_n} \right) \\
D_{k_n} &= \| \mathbf{C}_{k_n(n)} - \mathbf{S}_{k_n(n)} \| \\
{}^{w}\mathbf{T}_m &= \begin{bmatrix} {}^{w}\mathbf{R}_m & {}^{w}\mathbf{t}_m \\ 0 & \frac{1}{s} \end{bmatrix}
\end{aligned}
\tag{3.5}
$$

where ${}^{w}\mathbf{T}_{m}^{t}$ $(s, {}^{w}\mathbf{R}_{m}, {}^{w}\mathbf{t}_{m})$ indicates the transformation matrix from the ^{m}RF in the ^{w}RF, composed of rotation, translation and scaling factor, $||\dots||$ is the Euclidean distance, $\mathbf{C}_{k_n(n)}$ and $\mathbf{S}_{k_n(n)}$ are respectively the 3D point on the contour line and the 3D point of the silhouette of the model.

A GA optimization process is performed independently on each frame, to avoid local minima [31]. The population is composed of the parameters that define the pose of the femur in the world reference frame, i.e. Euler angles, translation vector and scaling. The initial population (40 samples) of each minimization is extracted from uniform parameter distributions defined as small deviations $(\pm 10^{\circ}, \pm 10mm, \pm 0.1scalefactor)$ from an initial pose, i.e. the initialization pose for the first frame or the result of the previous minimization otherwise. The maximum number of iterations was equal to 100. However, the minimum was found before reaching the maximum number of iterations.

Shape optimization

After the first optimization of the pose, we performed a shape optimization, based on the algorithm described in [74]. The shape optimization process implemented a closed form solution for the best approximation of the original shape with a deformable model. The optimization is inserted in a minimization procedure F_{shape}, based only on the $O-1=23$ weights of the SSM (α_o).

$$
\begin{aligned}
F_{shape} &= \min_{\alpha_o} \left(\sum_{k_n=1}^{K_n} D_{k_n} \right) \\
D_{k_n} &= \| \mathbf{C}_{k_n(n)} - \mathbf{S}_{k_n(n)} \|
\end{aligned}
\tag{3.6}
$$

3.2.4 Validation

Datasets

In order to validate our tracking algorithm we used the datasets of three different patients, which have respectively severe, mild and moderate osteoarthritis of the knee. For each patient, we have the CT scan and we generate the DRRs. The difference in the grade of osteoarthritis for the

three subject is evidenced by an increased number of osteophytes from mild to moderate and severe that is reflected in a more deformed femur. This causes the printed silhouette to be also deformed, and is reflected in a lower capability of registration compared to healthy subjects.

The CT dataset was composed of DICOM images acquired with a SIEMENS Sensation 64 CT machine. Each slice is 512x512 pixel (0.3516 mm/pixel) with a slice thickness of 0.6 mm and a spacing between slices of 0.4 mm. In order to assess the model reconstruction performance we segmented the bone shape using Amira® (VSG|FEI, France).

For each patient, a virtual environment around the CT was created, in order to simulate fluoroscopic scans from three different point of views. 11 angles of flexion were simulated for a total of 11 x 3 patients x 3 views = 99 images. The center of the CT dataset was taken as the ^{w}RF. The setup of the acquisition was virtually created in order to have the ground truth for the pose of the femur. The DRR is built integrating the density of each voxel of the CT along the direction of each ray as in [52]. Three different sources and image planes were simulated for each patient, resulting in three sets for each patient: the first image shows a lateral view of the femur (L_0), the second and third images show a view rotated on the sagittal plane of 10 (L_{10}) and 90 degrees (F) (see Figure 3.6). In this way, we can compare how the results are influenced by the angle of view of the projection. A lower angle is expected to give problems in depth definition, but allows us to understand if a registration with a single plane projection is feasible or not.

To represent the knee flexion-extension, we rotated the images T times ($t = 0, ..., T$, with $T = 10$). The pose of the CT shape is fixed and the source and the image plane rotate in order to simulate a rotation of the femur. To build the images on the lateral plane, we rotated the image plane of 8° clockwise. The same rotation is made on the frontal plane, rotating both the image and the source, to get a consistent motion of the femur in the 3D space (see Figure 3.7).

Experimental protocol

To reduce the computational effort of the minimization function, we used 3D models with a reduced number of points (1:8). The reduction was done iteratively collapsing the shortest edge to one point, in order to pre-

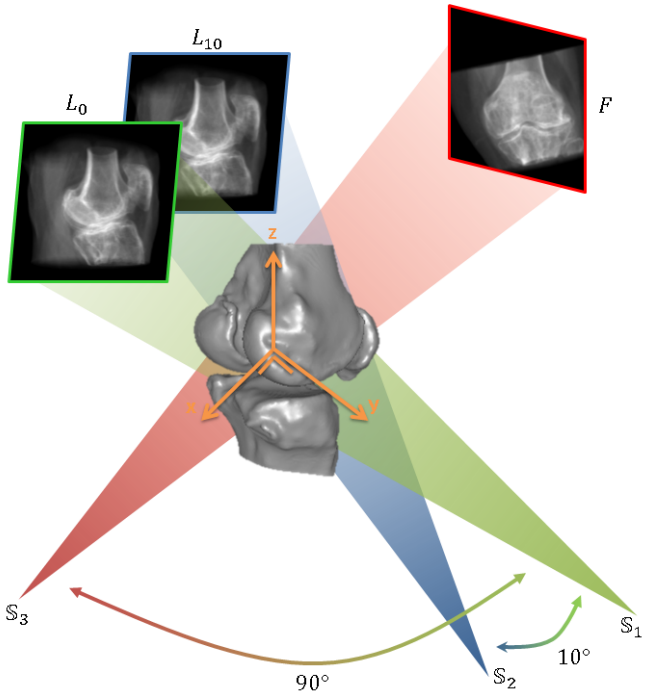

Figure 3.6: *Description of the virtual environment setup for the DRR creation. The CT model reference frame was used as world reference frame (orange reference frame). The source of L_0 was established on the y-axis, as well as the center of L_0. L_{10} is obtained rotating the source-plane axis of 10 degrees on the x-y plane. F is obtained rotating the source-plane axis of 90 degrees, having it correspondent to the x-axis [57]*

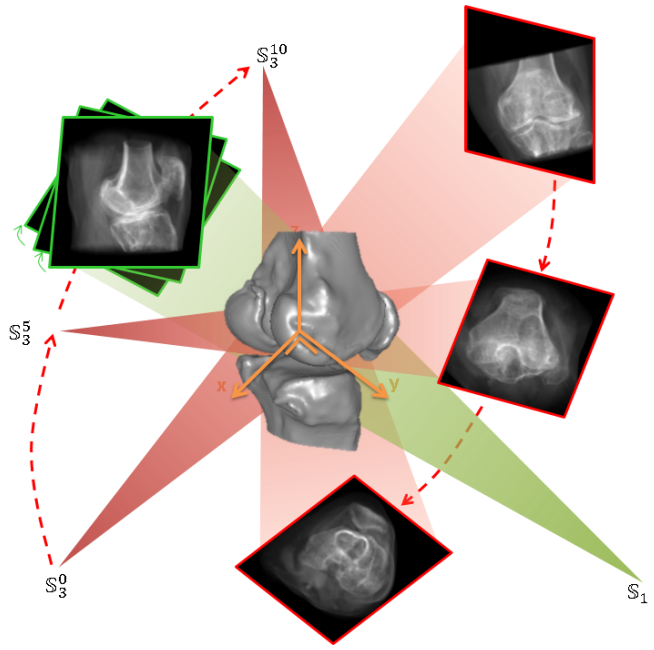

Figure 3.7: *Description of the virtual environment setup for the DRR creation. To represent the knee flexion-extension, we rotated the images T times of 8 degrees each ($T = 10$). $\mathbf{S}_3^0$ indicates the position of the source of image 3 at time 0, $\mathbf{S}_3^5$ indicates the position of the source of image 3 at time 5 and $\mathbf{S}_3^{10}$ indicates the position of the source at time 10, i.e. after 80 degrees of rotation from time 0*

serve the structure of the shape. Eight times was found to be the correct threshold between a considerable reduction of time and an acceptable shape to compare the silhouette to the contour. In order to evaluate the performance of the shape reconstruction and the tracking separately, we used the CT-based shape and the SSM shape. An open source software called Cloud Compare (www.danielgm.net/cc) was used to assess the differences between the SSM and the CT shape. The software returns both the point to shape distances for the meshes (calculated as the distance between points and facets) and a graphical view of them. Referring to Figure 3.6, we call L_0 the lateral view (Image 1 in the figure), L_{10} the projection at 10 degrees (Image 2 in the figure) and F the frontal view (Image 3 in the figure). The tracking algorithm was then computed on the following images sets:

- $CT(L_0 - L_{10})$: Tracking is done using the CT shape and images L_0 and L_{10}.
- $CT(L_0 - F)$: Tracking is done using the CT shape and images L_0 and F.

- $SSM(L_0 - L_{10})$: Tracking is done using the SSM shape and images L_0 and L_{10}.
- $SSM(L_0 - F)$: Tracking is done using the SSM shape and images L_0 and F.

These four setups are tracked for each one of the three models from which the DRR were generated. Kruskal-Wallis test $p < 0.05$ was performed to verify the significant difference between the median of each test.

3.3 Results

We tested the capability of the algorithm to deform the SSM in order to better approximate the CT shape and the ability to reconstruct the pose of the femur with two images per sample time.

In most cases, the distance between the SSM and CT was less than 3mm (Figure 3.8 and Table 3.2)

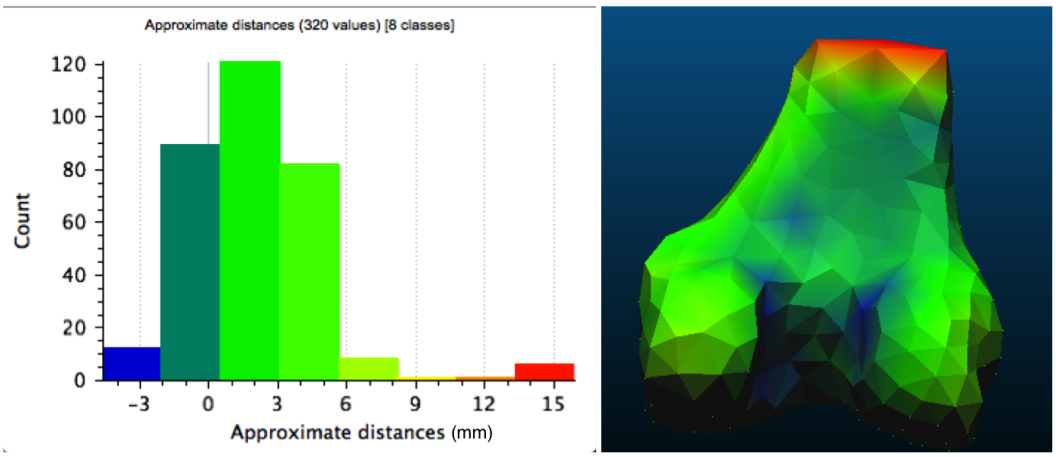

Figure 3.8: *Similarity between the original CT mesh and the reconstructed SSM mesh*

Table 3.2: *Mesh comparison statistical parameters: distances from point to surface represented as mean and standard deviation*

	DRR 1	DRR 2	DRR 3
$SSM(L_0 - L_{10})$	$0.516 \pm 2.438mm$	$-0.607 \pm 5.104mm$	$2.188 \pm 2.933mm$
$SSM(L_0 - F)$	$0.545 \pm 2.391mm$	$-0.418 \pm 4.955mm$	$2.066 \pm 2.835mm$

For each CT shape we identified the anatomical axis (as defined in [53]) and used these axis to report the errors.

As in [13], we defined the **precision** as the standard deviation of the remaining error after removing the mean error of all frames for that specific sequence. Difference in coordinate system definition is thus minimized, as it is mainly formed by mean error. The three sequences (one for each patient) are than considered as a single population. In Figure 3.9 the boxplots of the angular precision for each anatomical axis are shown, while in Figure 3.10 the translation precision on each axis are shown. Kruskal-Wallis test was performed to verify the significant difference between the median of each test.

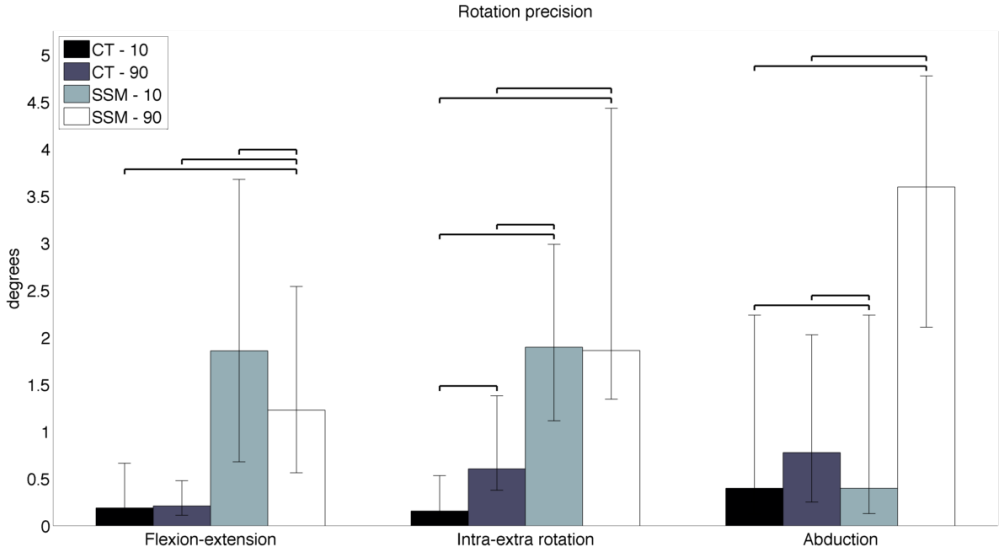

Figure 3.9: *Rotation precision with respect to the ground truth (known as artificially generated). The height of the box indicates the median value and whiskers extend from the 25th to the 75th percentile. Square parenthesis above two boxes indicates that the two populations are statistically different.*

3.4 Discussion

In this paper, we present a femoral kinematics reconstruction technique based on biplane fluoroscopic images taken during knee flexion-extension movements using SSMs.

The tracking capabilities of the proposed method were separately evaluated using the exact model, semi-automatically reconstructed from the CT dataset, and the implemented SSM [68].

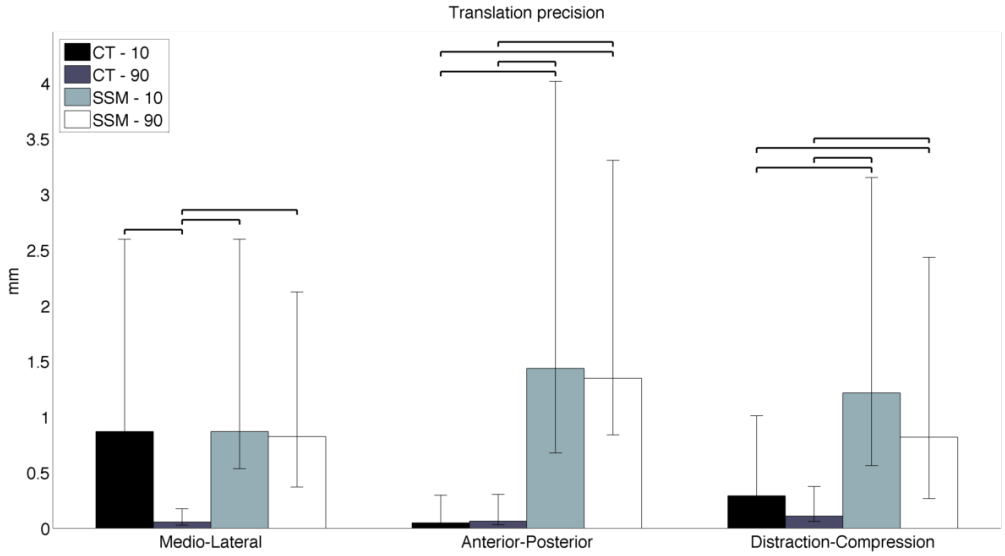

Figure 3.10: *Translation precision with respect to the ground truth (known as artificially generated).*

Our approach shows the applicability of a semi-automatic algorithm for 2D/3D registration using SSM. With respect to dynamic MRI, our method is less expensive and more accurate [35]. Compared to actual clinical procedures, that are based on a previous static CT or MRI scan and a manual fitting of the shape, this method is less expensive (as CT and MRI can be avoided) and more accurate due to the automatic fitting. The ionizing radiation given to the patient in our procedure is just a few hundredths of a mSv (considering a total of 22 images and an average dose of 0.001mSv for each image, we have a total dose of 0.02mSv, much lower than a 2.2mSv average dose absorbed with a CT) [4, 40]. Compared to skin mounted markers, our system does not suffer from relative movements between the skin and the bone, and is thus suitable for accurate joint kinematics studies [20, 42, 47]. Our method proved to be stable without relying on implanted markers or joint implants, that will return more accurate results at the price of high invasiveness [60–62].

In order to have the ground truth pose of the model, we artificially simulated the fluoroscopic projections using DRR technique. Our SSM was derived using 24 MRI datasets of healthy patients. Such a number of samples is quite limited compared to other datasets in the literature e.g. [11] used 43 CT images of the knee and [74] used 30 CT-based

models of the hip. When we evaluated the exact model reconstruction ability of our SSM and the implemented deformation technique we found residual errors on the order of 2.2 mm as median Euclidean distance in the worst case. Such error is due to the different levels of cut of the femoral diaphysis and to the limited number of femurs used as SSM. Also, the subject used to obtain the DRRs were osteoarthritic, thus with evident deformity of the femur's shape. The result obtained is in line with the ones by [11], where they state a point to surface distance of 2 mm and maximum errors of 3 mm. Having a larger dataset, including greater variations, would allow increasing the morphing possibilities, reducing reconstruction errors.

In the case of the CT shape, all the median translation errors are lower than 1 mm, in line with the results presented by [11]. We used two differents angles for the DRR definition, and the results showed that the higher translation error in medio-lateral precision at 10° is due to a lower capability to resolve the depth information. The residual error at 90° can be associated to rounding error and to a limited number of generations for each GA running.

Using the SSM shape the results are statistically different from the one obtained with the CT shape. The translation median errors are lower than 1.5 mm, probably due to the low deformation possibilities given by the reduced number of shapes of the training set, whereas the rotation error spans up to 4° in almost all directions. In [13] the authors state errors up to 3° but they used a SSM including a longer femoral diaphysis, thus the informative content of the statistical model is bigger.

The advances of the proposed new methodology with respect to the current state of the art resides in the fact that our method has been applied to pathological patients resulting in accuracy comparable to the current state of the art. Moreover, we managed to achieve limited decrease in performance with a lower angle (up to 10°) between the fluoroscopic projections. In this way, the range of movement for the flexion-extension of the knee is enlarged, extending the possibilities for the tracking with different movements.

One of the limits of our study is the reduced testing dataset for tracking, nevertheless since we used 11 image projections, progressively extending the knee joint, the dataset is enough to assess the statistical power

of the analysis. Fluoroscopic images could be much noisier than the virtually reconstructed projections, due to fast acquisition of the images that causes blurring, calibration plates and white noise due to instrumentation. Further analysis will be directed towards adding realistic noise to the images and testing the tracking algorithm performances. Acquired images as performed in [57] will also be used to test the algorithm.

In conclusion, we showed the clinical applicability of our method for femoral tracking using a biplane fluoroscopy and based on SSM, thus reducing costs and lowering the patient's radiation dose.

CHAPTER 4

Femur kinematics registration based on Gaussian Mixture Models

This work was submitted to the Journal of Medical and Biological Engineering and computing with the title "Gaussian Mixture Models based 2D-3D registration of bone shapes for orthopaedic surgery planning" and has been accepted for publication.

4.1 Introduction

Osteoarthritis is a highly debilitating pathology that affects knees primarily of older people. With this inflammation, the cartilage degenerates, the distance between bones is reduced and hypertrophy of the bones can occur, with the creation of osteophytes [72]. The Dutch Institute for Public Health estimates that worldwide almost 16% of men and 31% of women aged over 55 years have radiographic knee osteoarthritis [49]. In 12% of cases the pathology reduces the motion of the knee and causes pain to the patient, often requiring the use of ambulatory aids [17]. The most used treatment for severe osteoarthritis is surgery. Almost the 20% of the patients that undergo Total Knee Arthroplasty (TKA) are not satisfied with their operation [8].

A pre-operative study of knee kinematic under weight-bearing conditions can improve the outcome of the surgery [65]. The representation of the joint kinematics in 3D space allows for understanding pain zones and ligament tension, determining the best implant positioning and thus correcting non-alignments of the bone segments [12, 14, 15, 32, 63, 65, 76]. The acquisition of pre-operative Computed Tomography (CT) or Magnetic Resonance Imaging (MRI) images gives a deep insight into the morphology of the structures, but these procedures are currently limited to static positioning and have high costs and radiation doses given to the patient. Mono and multi-plane fluoroscopy are the most accurate and used procedures to measure in vivo non-invasive kinematics of the knee [65, 76]. The current clinical technique is mainly based on the operator's ability to correctly position the shape on the images [8]. This technique is time-expensive and error-prone, as it is based on human ability. Regardless of the number of fluoroscopic projections, two main automatic methods have been implemented to recover the correct pose of the bones in 3D space: intensity based and feature based methods.

Intensity based methods need a pre-operative CT scan in order to acquire the density of the patient's bone. The 2D-3D matching is then achieved comparing the Digitally Reconstructed Radiograph (DRR) to the acquired fluoroscopic image and adjusting the rotation and translation parameters in order to minimize the differences between the two images in terms of pixel intensities [9, 34, 65]. Although very accurate, these methods require a previous CT to determine the bone density for the DRR creation, and are computationally expensive for the number of pixel intensity comparisons that must be made to find the correct pose.

Feature based methods are based on the contours of the bone shape that can be extracted from the fluoroscopic images using edge detector filters, such as Canny or Sobel [19, 44, 45]. These methods project the silhouette of the bone shapes and match it with the extracted edges. Usually, feature based methods necessitate a previous morphological 3D dataset of the bone shapes, such as MRI or CT [7, 8, 62]. Recently, some authors have addressed the problem of needing the morphological scan and substituting it with a Statistical Shape Model (SSM), a collection of shapes coming from atlas that can be deformed in order to represent accurately the target shape [12, 67, 74]. In this way, costs are reduced and

the patient is exposed to a lower radiation dose. However, computation time becomes an issue, as the whole sequence of poses takes some hours to be computed [13].

The aim of this chapter is to solve a well-known registration problem of 3D shapes on 2D images. The issue is addressed using Gaussian Mixture Models (GMMs), a technique already present in literature but not currently used to solve this type of problems. We tested the algorithm with a SSM of the femur using a set of fluoroscopic images of the knee. The goal is twofold: we addressed the problem of accurately recovering the pose of the knee in 3D space in a completely automatic way and also of ensuring the correct parameters for the deformation of the shape. In [43, 73], the authors addressed the problem of the registration of two point-sets with a GMM fitting. The solution is given through an Expectation Conditional Maximization (ECM) procedure, that simplifies the original Expectation Maximization (EM) algorithm by Dempster et al. [33]. Both of these frameworks, however, assume working with point-sets lying in the same (2D or 3D) space.

The proposed algorithm extends the state of the art to registering a 3D shape of a femur on a set of fluoroscopic images acquired during flexion-extension of the knee.

4.2 Materials and methods

The knee is imaged during a sequence of flexion-extension movements. A fluoroscopic tube returns a set of X-ray images. The source and the image plane are calibrated, and their pose in the world reference frame is known. The reconstruction of the femur kinematics is done through a series of features projection and back-projection from the fluoroscopic image plane to the 3D space. A 3D shape of the bone is used as a model to reconstruct the correct pose (see Figure 4.1).

4.2.1 Datasets

2D contours

The segmentation of the contour of the shape ${}^{j}\mathbf{y}_n$ on each fluoroscopic image I_j is performed using a semi-automatic algorithm based on gradient enhancement of the image and a spline interpolation between user

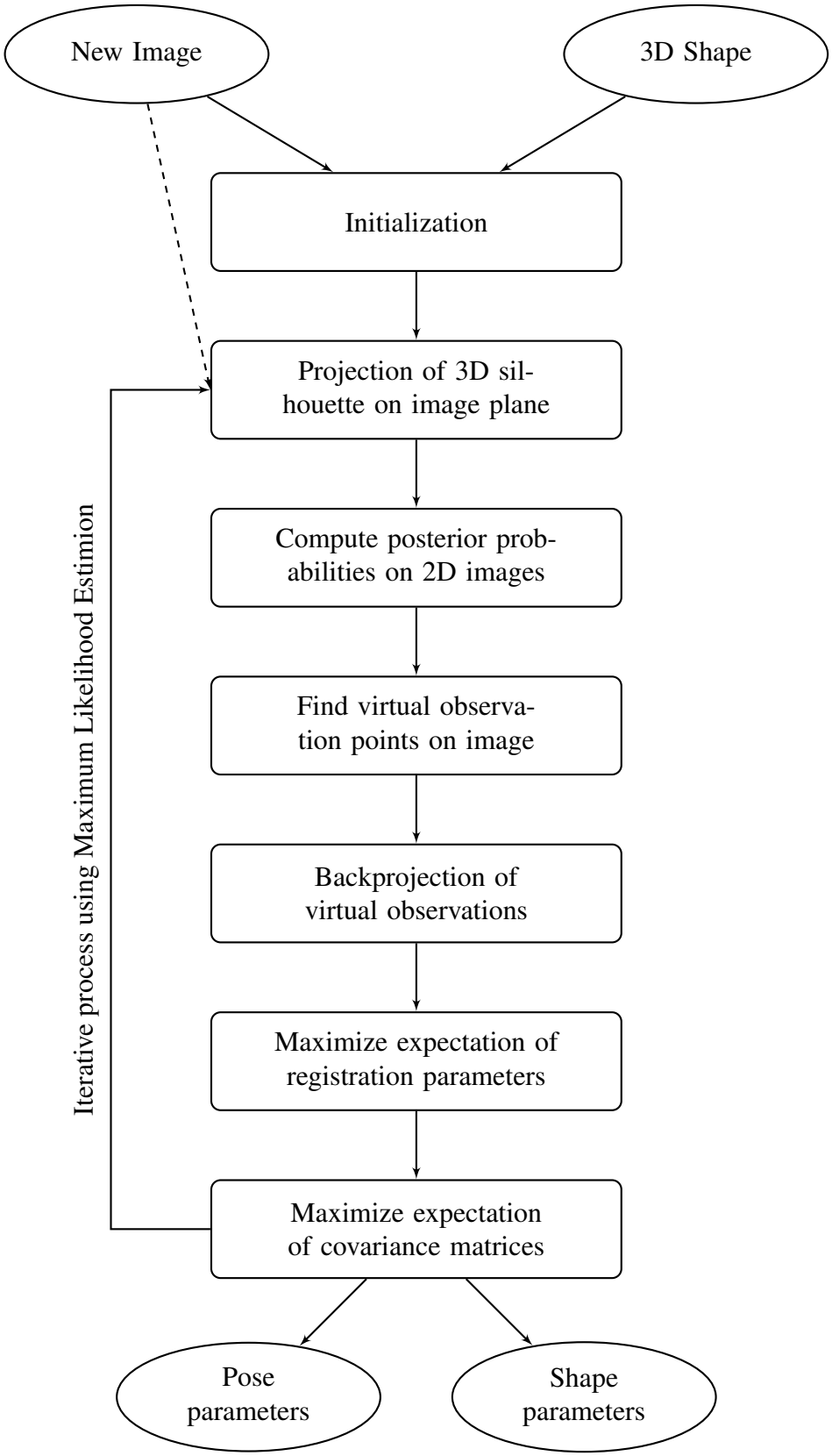

Figure 4.1: *Flowchart of the GMM based algorithm.*

picked points [67]. The selected pixels, belonging to the segmentation, can be transformed in 3D points using the known image calibration parameters ($\mathbf{y}_n, n = 1, \ldots, N$).

3D shape

The 3D shape is defined as a set of points ($\mathbf{X}_s, s = 1, \ldots, S$) and triangles that can be either derived from the segmentation of a volumetric image dataset (CT or MRI) [50] or a SSM [22]. We define the patient specific 3D shape as 3D$S_{CT/MRI}$ and the SSM as 3DS_{SSM} (chapter 2). A Gaussian distribution ($\mathbf{X}_s, \mathbf{\Sigma}_s$) is associated to each 3D point of the model. The isotropic covariance can be expressed as:

$$\mathbf{\Sigma}_s = \sigma_s \mathbf{I}_3 \tag{4.1}$$

where $\mathbf{I}_3$ is the 3×3 identity matrix and σ_s is the scalar value of the covariance that varies for each $\mathbf{X}_s$ point.

2D silhouette

The silhouette of the model is made up of those points that share a contour edge, i.e. an edge shared by two facets with normals pointing in different directions from the source. The silhouette points are then a subset of the shape points $\mathbf{X}_m, m = 1, \ldots, M < S$. The model silhouette is projected on the image plane ${}^j\mathbf{x}_m, m = 1, \ldots, M$ where j indicates the image on which the points are projected. We also define a set of virtual observations ${}^j\mathbf{o}_m$ that have a correspondent point in the 3D space $\mathbf{O}_m$.

4.2.2 Registration

The registration problem is the estimation of the homogeneous matrix (expressed by the transformation parameters θ) which minimizes the distance between the virtual observation $\mathbf{O}_m$ and the silhouette point $\mathbf{X}_m$. The description of the algorithm is summarized in 1.

The variables used in this description are:

- ${}^j\mathcal{Y}$ is the contour extracted from each image, whose pixels are ${}^j\mathbf{y}_n, n = 1, \ldots, N$ (also called observations)
- $\mathbf{X}_s, s = 1, \ldots, S$ are the points of the 3D shape

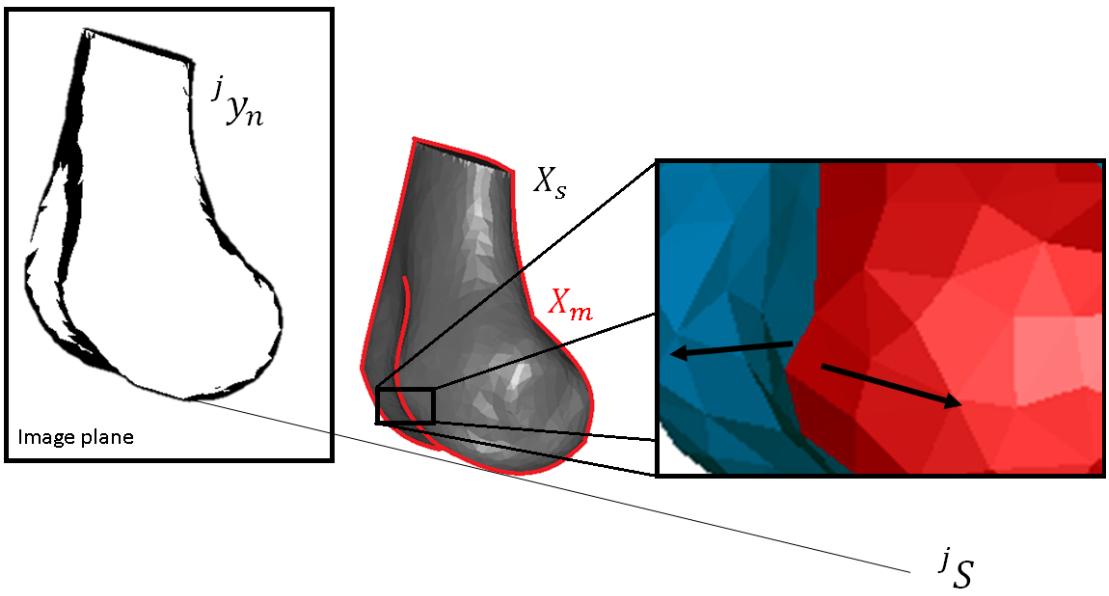

Figure 4.2: *The X-ray source ^{j}S projects rays on the image plane. The image is processed and the contours $^{j}y_n$ are extracted using a Canny edge detector (black points on the image). In the middle, the shape is formed by points X_s and triangles. The silhouette of the model, X_m in red, is made up of those points that share a contour edge, i.e. an edge shared by two triangles with normals (arrows) pointing in different directions from the source. The zoom on the right shows the normals of the triangles that point in different directions.*

- $^{j}\mathcal{X}$ is the set of points of the silhouette $^{j}\mathbf{X}_m, m = 1, \ldots, M < S$
- $^{j}\mathbf{x}_m, m = 1, \ldots, M$ are the pixel of the shape's silhouette projected on image j
- $^{j}\mathbf{o}_m, m = 1, \ldots, M$ are the virtual observations on the image j
- $\mathbf{O}_m, m = 1, \ldots, M$ are the virtual points backprojected in the 3D space

Initialization

A manual initialization is necessary to define the initial pose for the shape. Seven landmark points $L_i, i = 1, \ldots, 7$ are identified on the 3D shape 3DS. The user is asked to select the same points on the images [68]. The backprojected lines from the user-selected points to the corresponding source identify seven landmarks in the 3D space. Using corresponding points registration [10], we find the homogeneous transformation matrix $\mathbf{T}$ that maps the shape in the calibrated image space.

The accuracy in finding the exact points on the images, and the resulting initialization matrix T is not crucial, as the whole algorithm has been proven to be robust against initialization: we checked the robustness of the method initializing the algorithm with different poses, starting from the correct pose and gradually adding up to 5 cm and 5° of uniform random noise to the correct matrix. The results showed that with an error higher than 2 cm and 2° the system is not assured to converge, while with a lower error the system converges with final errors lower than 1 mm. The initialization can thus be considered independent from the operator's skills.

Gaussian Model and Likelihood

Each $\mathbf{X}_s$ point of the model is defined as the centroid of a 3D Gaussian distribution with mean $\mathbf{X}_s$ and covariance matrix $\mathbf{\Sigma}_s$, identifying in this way a Gaussian Mixture Model (GMM). The operator $\mu : \mathbb{R}^3 \rightarrow \mathbb{R}^3$ transforms a point $\mathbf{X}_s$ in another point $\mu(\mathbf{X}_s, \theta)$ where θ is the parameterization of the transformation.

The likelihood ($\mathcal{L}$) that expresses the probability that the contour is coincident with the silhouette projection is a function of both the registration parameters θ and the covariances.

$$\mathcal{L}(\theta, \sigma_1, \ldots, \sigma_S \,|\, \mathcal{Y}) = \log \mathcal{P}\left(\mathcal{Y}; \theta, \sigma_1, \ldots, \sigma_S\right) \tag{4.2}$$

where $\mathcal{P}\left(\right)$ is the probability that the set of observations $\mathcal{Y}$ is extracted from the GMM with parameters (θ, σ) and the likelihood indicates the probability that the set of observations $\mathcal{Y}$ is coincident with the projection of the shape's silhouette $\mathcal{X}$.

This maximization can not be performed due to the presence of missing data, as the assignment of each observation to one of the Gaussian of the GMM is unknown. The operator $\{Z : \mathbf{y}_n \rightarrow \mathbf{x}_m\}, n = 1, \ldots, N$ assigns an observation $\mathbf{y}_n$ either to a silhouette model point $\mathbf{x_m}$ or to an outlier class. If $(Z : \mathbf{y}_n \rightarrow \mathbf{x}_m)$ then the observation $\mathbf{y}_n$ is associated to the point $\mathbf{x}_m$, otherwise, if $(Z : \mathbf{y}_n \rightarrow \mathbf{x}_{M+1})$ then the observation $\mathbf{y}_n$ is an outlier.

The likelihood is replaced by the expected complete-data log-likelihood $\mathcal{E}$ conditioned by the observed data, as suggested by Dempster [33].

$$\mathcal{E}(\theta, \sigma_1, \ldots, \sigma_S \,|\, \mathcal{Y}, Z) = E_Z[\log \mathcal{P}\left(\mathcal{Y}, Z; \theta, \sigma_1, \ldots, \sigma_S\right) \,|\, \mathcal{Y}] \tag{4.3}$$

To evaluate eq (4.3) the probabilities of the observations must be expressed as a set of Probability Density Functions (PDFs).

$$p_m = \mathcal{P}\left(Z : \mathbf{y}_n \rightarrow \mathbf{x}_m\right)$$

is the prior probability that the observation $\mathbf{y}_n$ belongs to the cluster m with centre $\mu(\mathbf{x}_m; \theta)$ while $p_{M+1} = \mathcal{P}\left(Z : \mathbf{y}_n \rightarrow \mathbf{x}_{M+1}\right)$ expresses the prior probability of $\mathbf{y}_n$ to be an outlier.

$$p_m = \begin{cases} \mathcal{P}\left(Z : \mathbf{y}_n \rightarrow \mathbf{x}_m\right) = \frac{a}{A} & \text{if } 1 \leq m \leq M \\ \mathcal{P}\left(Z : \mathbf{y}_n \rightarrow \mathbf{x}_{M+1}\right) = \frac{A - Ma}{A} & \text{if } m = M+1 \end{cases} \tag{4.4}$$

In eq (4.4) the variable a indicates a small circular area $\left(a = \pi r^2\right)$ around the centre of the projected GMM $\mu(\mathbf{x}_m, \theta)$, whereas A indicates the whole volume of work, so that $a \ll A$. The likelihood of an observation $\mathbf{y}_n$ given its assignment to cluster m is drawn from a normal distribution:

$$\mathcal{P}\left(\mathbf{y}_n \mid Z : \mathbf{y}_n \rightarrow \mathbf{x}_m\right) = \mathcal{N}(\mathbf{y}_n \mid \mu(\mathbf{x}_m; \theta), \sigma_m) = \frac{1}{\sigma_m \sqrt{2\pi}} e^{-\frac{||\mathbf{y}_n - \mathbf{x}_m||^2}{2\sigma_m^2}} \tag{4.5}$$

and the same likelihood of the observation given its assignment to the outlier class is a uniform distribution over the area A

$$\mathcal{P}\left(\mathbf{y}_n \mid Z : \mathbf{y}_n \rightarrow \mathbf{x}_{M+1}\right) = \mathcal{U}(\mathbf{y}_n \mid A, 0) = \frac{1}{A} \tag{4.6}$$

The marginal distribution of an observation is:

$$\mathcal{P}\left(\mathbf{y}_n\right) = \sum_{m=1}^{M+1} p_m \mathcal{P}\left(\mathbf{y}_n \mid Z : \mathbf{y}_n \rightarrow \mathbf{x}_m\right) \tag{4.7}$$

Eq (4.2) then becomes

$$\log \mathcal{P}\left(\mathcal{Y}\right) = \sum_{m=1}^{M} \log \left(\sum_{n=1}^{N} p_n \mathcal{N}(\mathbf{y}_m \mid \mu(\mathbf{x}_n; \theta), \sigma_n) + \frac{p_{n+1}}{A} \right) \tag{4.8}$$

and eq. (4.3) becomes

$$\mathcal{E}(\theta, \sigma_1, \ldots, \sigma_S \mid \mathcal{Y}, \mathcal{Z}) = \sum_{\mathcal{Z}} \mathcal{P}\left(\mathcal{Z} \mid \mathcal{Y}, \theta, \sigma_1, \ldots, \sigma_S\right) \cdot \\ \cdot \log \mathcal{P}\left(\mathcal{Y}, \mathcal{Z}; \theta, \sigma_1, \ldots, \sigma_S\right) \tag{4.9}$$

Expectation Conditional Maximization

The Expectation Conditional Maximization method is an iterative way to solve the Maximum Likelihood problem of eq (4.3). Starting from an initial estimate of the parameters, the method computes the posterior probabilities given the current parameters and covariances and then maximizes the expectation in (4.3) with respect to the registration parameters (given the current covariances) and the covariances (given the newly estimated parameters).

The expectation step (E-step) involves the computation of the posterior probability p_{mn} that every point of the projected shape on the image plane ($\mathbf{x}_m, m = 1, \ldots, M$) is associated to a point of the contour ($\mathbf{y}_n, n = 1, \ldots, N$):

$$\begin{aligned} p^q_{mn} &= \mathcal{P}\left(Z : \mathbf{y}_n \rightarrow \mathbf{x}_m \,|\, \mathbf{y}_n; \theta^q, \sigma^q\right) = \\ &= \frac{\mathcal{P}\left(\mathbf{y}_n \,|\, Z : \mathbf{y}_n \rightarrow \mathbf{x}_m\right) \mathcal{P}\left(Z : \mathbf{y}_n \rightarrow \mathbf{x}_m\right)}{\mathcal{P}\left(\mathbf{y}_n\right)} = \\ &= \frac{\sigma_m^{-2} e^{\frac{-||\mathbf{y}_n - \mathbf{x}_m||^2}{2\sigma_m^2}}}{\sum_{i=1}^{M} \sigma_i^{-2} e^{\frac{-||\mathbf{y}_n - \mathbf{x}_i||^2}{2\sigma_i^2}} + c} \end{aligned} \tag{4.10}$$

where Z is the association operator between a projected point $\mathbf{x}_m$ of the shape's silhouette $\mathbf{X}_m$ with a point of the contour $\mathbf{y}_n$ extracted from the image, q is the current time and c is the outlier component:

$$c = 2r^{-2} \tag{4.11}$$

The set of unknown variables is composed by the registration parameters $\theta[6 \times 1] = \{q_1, q_2, q_3, t_1, t_2, t_3\}$ where $q_i, i = 1, 2, 3$ are the Euler angles and $t_i, i = 1, 2, 3$ are the translation values, and the set of 3D points variances $\sigma_1^2, \ldots, \sigma_M^2$:

$$\psi = (\theta, \sigma_1^2, \ldots, \sigma_M^2) \tag{4.12}$$

As the direct maximization of the likelihood is intractable, the minimization of the negative log-likelihood ($E(\psi)$) will instead be taken as the objective [33]:

$$E(\psi) = -\sum_{n=1}^{N} \log \sum_{m=1}^{M} \mathcal{P}\left(\mathbf{X}_m\right) \mathcal{P}\left(\mathbf{y}_n \,|\, \mathbf{X}_m(\theta; \sigma_m^2)\right) \tag{4.13}$$

The minimization function can thus be transformed in:

$$E(\psi) = \frac{1}{2}\sum_{n=1}^{N}\sum_{m=1}^{M}\frac{p_{mn}^{q}}{\sigma_m}\left[\left(||\mathbf{y}_n - \mathbf{X}_m(\theta)||^2\right) + 3\sigma_m^2\log(\sigma_m^2)\right] + \frac{\rho}{2}||L(\phi)||^2 \tag{4.14}$$

where $||L(\phi)||^2$ is a regularization parameter over the transformation, and ρ weights its contribution to the minimization.

The conditional maximization step aims at maximizing the likelihood described in eq. (4.2) and (4.3). It uses the definition of virtual observation, that is a normalized sum over all the observations weighted by their posterior probability [43]. The virtual observation O and its weight λ are obtained for each model point x_n using the posterior probabilities p_{mn}^{q} and the observations $\mathbf{y}_m$:

$$\begin{aligned} \nu_n &= \sum_{m=1}^{M} p_{mn}^{q} \\ \mathbf{o}_n &= \frac{1}{\nu_n}\sum_{m=1}^{M} p_{mn}^{q}\mathbf{y}_m \end{aligned} \tag{4.15}$$

Eq. (4.3) can be rewritten replacing the conditional probabilities with the normal and uniform distribution as expressed in eq (4.16) (for the complete steps the reader can refer to [43])

$$\mathcal{E} = -\frac{1}{2}\sum_{m=1}^{M}\sum_{n=1}^{N}\frac{p_{mn}^{q}}{\sigma_n^2}(||\mathbf{y}_m - \mu(\mathbf{X}_n,\theta)||^2 + \log(\sigma_n^2)) \tag{4.16}$$

The minimization of eq (4.16) over θ keeping constant the covariances σ lead to:

$$\theta^{q+1} = \arg\min_{\theta}\frac{p_{mn}^{q}}{\sigma_n^2}||\mathbf{y}_m - \mu(\mathbf{X}_n,\theta)||^2 + \frac{\rho}{2}||L(\mu)||^2 \tag{4.17}$$

where $||L(\mu)||^2$ is a regularization term over the parameters. Eq (4.17) can be simplified using the definitions of eq (4.15):

$$\theta^{q+1} = \arg\min_{\theta}\nu_n||\mathbf{O}_n - \mu(\mathbf{X}_n,\theta)||^2 + \frac{\rho}{2}||L(\mu)||^2 \tag{4.18}$$

where $\mathbf{O}_n$ is the 3D point nearest to $\mathbf{X}_n$ on the ray backprojected from $\mathbf{o}_n$. A 2D/3D registration problem is now cast into a 3D/3D registration that can be solved using already addressed solutions [10, 16, 43, 73].

The second step of the conditional maximization is the update of the covariances, using the registration parameters newly computed:

$$(\sigma_n^2)^{q+1} = \frac{\sum_{m=1}^{M} p_{mn}^q ||\mathbf{y}_m - \mu(\mathbf{x}_n, \theta^{q+1})||^2}{2 \sum_{m=1}^{M} p_{mn}^q} \tag{4.19}$$

In eq (4.19) the value $\mu(\mathbf{x}_n, \theta^{q+1})$ is the projection of the 3D point $\mathbf{X}_n$ updated with the parameters θ^{q+1}.

In the case of a rigid transformation, the parameter $||L(\phi)||^2$ is equal to 0, and the solution of the problem is given by a least-squares fitting of two 3D point sets, as described in [10].

If the shape to be registered is a 3DS_{SSM}, the parameters to be estimated are the shape coefficient vectors β_k, and the regularization term assumes the form of the Mahalanobis distance, with λ_k^2 eigenvalues of the SSM:

$$||L(\phi)||^2 = \sum_{k=1}^{K'} \frac{\beta_k^2}{\lambda_k^2} \tag{4.20}$$

All the shape coefficients are determined with a closed form solution as described in [73].

The algorithm converges to a minimum if the percentage difference between the likelihood of two consecutive frames is below a predefined threshold. Specifically:

$$\frac{\mathcal{L}^{(t)}(\mathcal{X} \,|\, \mathcal{Y}) - \mathcal{L}^{(t-1)}(\mathcal{X} \,|\, \mathcal{Y})}{\mathcal{L}^{(t-1)}(\mathcal{X} \,|\, \mathcal{Y})} < \epsilon \tag{4.21}$$

where $\mathcal{X}$ and $\mathcal{Y}$ are respectively the GMM and the observations. The likelihood of the current step is defined as:

$$\mathcal{L}(\mathcal{X} \,|\, \mathcal{Y}) = \prod_{n=1}^{N} \sum_{m=1}^{M} \alpha_m \cdot \left(\sigma_m^{-2} e^{\frac{-||\mathbf{y}_n - \mathbf{x}_m||^2}{2\sigma_m^2}} \right) \tag{4.22}$$

In (4.22), α_m is the component prior of the specific model [28].

4.2.3 Validation protocol

Twenty-four healthy knees were imaged with MRI scans and manually segmented to find the 3D shape. Those shapes were used to define the

Algorithm 1 GMM-based registration

procedure INITIALIZATION
    Extract contours from figure y_n
    Select landmarks on images L and find initialization matrix $\mathbf{T}$
procedure REGISTRATION
    procedure RIGID TRANSFORMATION
        loop:
        procedure E-STEP
            Project silhouette points $x_m \leftarrow X_m$
            Calculate posterior probability $p_{mn} = \mathcal{P}\left(Z(y_n = x_m(\theta, \sigma_m^2)) \,|\, y_n\right)$
        procedure CM-STEP (3D$S_{CT/MRI}$)
            Find virtual observations o_m
            Backproject virtual observations O_m
            Compute registration parameters θ
            $\sigma \leftarrow$ *update variance*
        goto *loop*.
    if Shape = SSM **then**
        procedure SSM ADAPTATION
            loop:
            procedure E-STEP
            procedure CM-STEP (3DS_{SSM})
                Find virtual observations o_m
                Backproject virtual observations O_m
                Compute shape deformation parameters β
                $\sigma \leftarrow$ *update variance*
            goto *loop*.
for all images **do**
    procedure RIGID TRANSFORMATION

SSM as described in chapter 2 [68].

The subject dataset is the following (Table 4.1):

- one healthy subject S_0 who underwent a CT scan (Sensation Cardiac 64, Siemens). The CT dataset is composed of 59 slices of 512×512 pixels each (0.7890625 mm/pixel). The slice thickness is 2 mm and the space between slices is 1.7 mm. The CT dataset was used to generate the DRR for evaluation purposes.

- Seven osteoarthritic patients ($S_i, i = 1, \ldots, 7$) eligible for TKA with different grades of osteoarthritis. The patients underwent a preoperative CT scan from which the 3DS_{CT} of the femur was segmented [41]. The CT datasets were composed of DICOM images acquired with a SIEMENS Sensation 64 CT machine. Each slice is 512x512 pixel (0.3516 mm/pixel) with a slice thickness of 0.6 mm and a spacing between slices of 0.4 mm. All the patients were also imaged at seven fixed flexion angles using two sequential fluoroscopic projections with an AXIOM Luminos dRF flat-bed (Siemens; Berlin, Germany) [8]. The first image was taken with the projector placed horizontally (lateral image), while the second was taken with the source at 10° below horizontal. Both projections were calibrated using custom made calibration software [57]. The fixed flexion angles ($0^\circ, 15^\circ, 30^\circ, 45^\circ, 60^\circ, 75^\circ, 90^\circ$) were obtained using steps of different customized heights on which the subject could step up. Three subjects (S_1, S_2, S_3) with different grades of osteoarthritis were selected to generate the DRRs of diseased knees.

  All the patients signed an informed consent and the institutional review board approved the study.

Subject	Age	Gender	Osteoarthritic grade	CT	$\text{DRR}_{0/10/90}$	$\text{Fluoroscopies}_{0/10}$
S_0	47	F	none	x	$0° : 3° : 72°$	
S_1	67	M	severe	x	$0° : 8° : 80°$	$0° : 15° : 90°$
S_2	75	M	mild	x	$0° : 8° : 80°$	$0° : 15° : 90°$
S_3	82	F	moderate	x	$0° : 8° : 80°$	$0° : 15° : 90°$
S_4	65	F	mild	x		$0° : 15° : 90°$
S_5	75	M	severe	x		$0° : 15° : 90°$
S_6	71	F	moderate	x		$0° : 15° : 90°$
S_7	82	M	mild	x		$0° : 15° : 90°$

Table 4.1: *For each subject, the age, gender and osteoarthritic grade are indicated. All the femurs analysed were right femurs. The $\text{DRR}_{0/10/90}$ values indicate the angles for which we generated the DRRs. We specify the starting and ending angle, with the step used. The $\text{Fluoroscopies}_{0/10}$ values indicate the angles of the fluoroscopic images.*

In order to assess the model reconstruction performances all the CT datasets were segmented using Amira® (VSG|FEI, France) and the anatomical reference frame was defined as in [53].

The DRR is built integrating the density of each voxel of the CT along the direction of each ray as in [52]. Three different sources and image planes were simulated for each patient, resulting in three sets for each patient: the first image shows a lateral view of the femur (L_0), the second and third images show a view rotated on the sagittal plane of 10 (L_{10}) and 90 degrees (L_{90}) (see Figure 4.3) [71]. For Subject S_0 we rotated the femur from $0°$ to $72°$ with a step of $3°$ generating the ground truth pose ($\mathbf{T}^i_{GT_0}, i = 0°, 3°, \ldots, 72°$). The three pathological DRRs were instead created rotating the femur from $0°$ to $80°$ with a step of $8°$ generating the ground truth pose ($\mathbf{T}^i_{GT_{1,2,3}}, i = 0°, 8°, \ldots, 80°$) [67]. The DRRs were generated by an academic partner and there was no possibility to select the angles of flexion.

Tests

The initialization is done as described in paragraph 4.2.2. The tracking consists in finding the correct pose of the 3DS for all the images provided for a given flexion sequence. The tests were performed with six different conditions $C_{1,\ldots,7}$:

C_1 : 3DS pose initialization with $D_0(0°)$ and $D_{90}(0°)$ and tracking with D_0 and D_{90} for all angles with $S_0, \ldots, S_3$

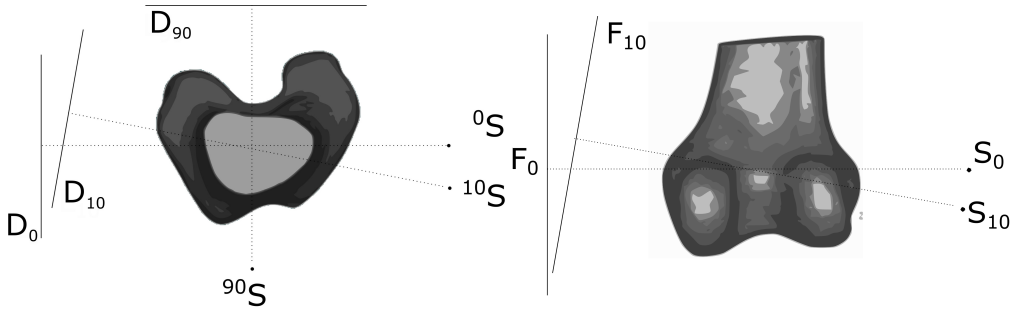

(a) *DRR creation* ***(b)*** *Fluoroscopy acquisition*

Figure 4.3: *Description of the virtual environment setup for the DRR creation and fluoroscopic acquisitions. The source S_0 was established on the medio-lateral axis, as well as the center of D_0 and F_0.*
For the DRR, D_{10} is obtained rotating the source-plane axis of 10 degrees on the horizontal plane. D_{90} is obtained rotating the source-plane axis of 90 degrees, having it correspondent to the antero-posterior axis.
For the fluoroscopies, F_{10} is obtained rotating the source-plane axis of 10 degrees on the medio-lateral axis.

C_2 : 3DS pose initialization with $D_0(0°)$ and $D_{90}(0°)$ and tracking with D_0 for all angles with $S_0, \ldots, S_3$

C_3 : 3DS pose initialization with $D_0(0°)$ and $D_{10}(0°)$ and tracking with D_0 and D_{10} for all angles with $S_0, \ldots, S_3$

C_4 : 3DS pose initialization with $D_0(0°)$ and $D_{10}(0°)$ and tracking with D_0 for all angles with $S_0, \ldots, S_3$

C_5 : 3DS pose initialization with $F_0(0°)$ and $F_{10}(0°)$ and tracking with F_0 and F_{10} for all angles with $S_1, \ldots, S_7$

C_6 : 3DS pose initialization with $F_0(0°)$ and $F_{10}(0°)$ and tracking with F_0 for all angles with $S_1, \ldots, S_7$

For each trial, both the SSM (3DS_{SSM}) and the CT segmented shape (3DS_{CT}) were used.

Results evaluation

The homogeneous matrix $\mathbf{T}_\theta^i$ was constructed from the optimal parameters θ returned by the ECM algorithm. In case of conditions $C_1, \ldots, C_4$, we computed $\mathbf{T}_{residual}^i = {\mathbf{T}_{GT}^i}^{-1} \cdot \mathbf{T}_\theta^i$. The errors were presented as rotations (in terms of Euler angles) and translations of $\mathbf{T}_{residual}^i$.

For the conditions $C_3, \ldots, C_6$, Edge to Surface (E2S) distance was computed [13]. E2S is defined as the Euclidean distance between a point on the 3D shape and the closest point on the associated contour pixel back projection. In this way, E2S does not require the ground truth pose to evaluate the accuracy of the algorithm. Kruskal-Wallis test with $p < 0.05$ was used to asses if the results for $C_3, \ldots, C_6$ using 3DS_{CT} and 3DS_{SSM} were statistically different.

4.3 Results

Figure 4.4 represents the results of an optimization of a 3DS_{CT} in C_1 condition. As shown in the figure, the points of the projected silhouette tend to overlay the points of the contour, in order to minimize the distance between the two datasets.

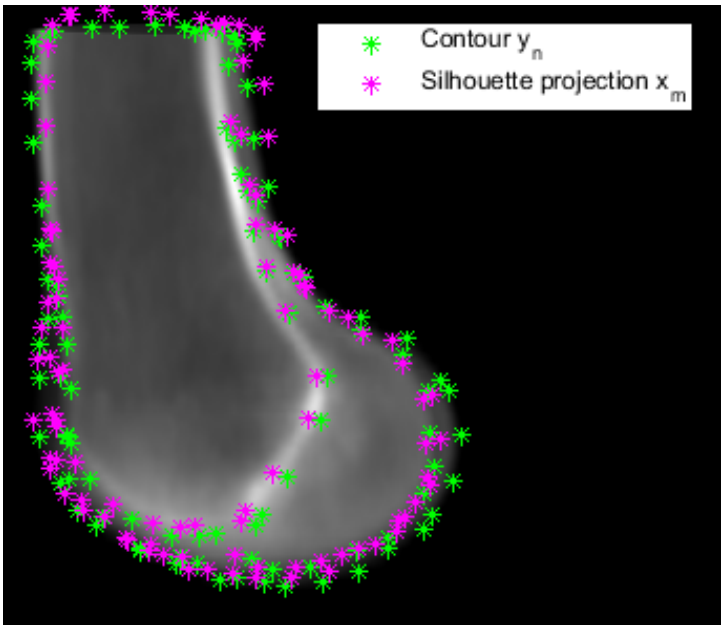

Figure 4.4: *Representation of the contour points and the silhouette points projected after the optimization of the algorithm*

In order to better understand the results, the errors have been expressed in the anatomical axes of the subject.

Figure 4.5 shows the values of rotation and translation of $\mathbf{T}_{residual}$ in the case of the healthy subject S_0. As can be seen, in case of single plane tracking or dual plane tracking with D_0 and D_{10} the error in the medio-lateral axis is increasing up to 3 cm with the flexion angle. The

translation errors on the other axis, as well as the rotation errors on every axis is bounded between some mm and 1 cm in the case of 3DS_{SSM}. The results are more accurate using the 3DS_{CT}. In this case, the errors are below 1 cm also in the out-of-plane axis (medio-lateral).

Figure 4.6 shows the errors in terms of rotation and translation for conditions $C_1, \ldots, C_4$ and using 3DS_{CT} and 3DS_{SSM}. In these figures it can be seen that the error is generally lower in the case of 3DS_{CT}, a part from the medio-lateral axis of S_2 when the error raises up to 6 cm. This is due to a very distal cut on the shaft of subject 2, that makes difficult the recognition of the correct pose of the shape. In S_3 an angle dependent trend is clearly visible, similar to those shown in Figure 4.5.

The edge to surface index is represented in Figure 4.7 for the only tests with L_0 and L_{10} images and for subject S_1, S_2, S_3. Results are presented as a populations of E2S Root Mean Square Error (RMSE) for each pose of the trials. Results were grouped for type of images analysed (DRR or fluoroscopies). The parenthesis above the boxplot indicate that Kruskal-Wallis test returned differences in the distribution median.

In Figure 4.8 are shown the E2S results for the fluoroscopic acquired images. Patients $S_1, \ldots, S_7$ proved to be statistically different only in a few cases, with S_2 that has the highest differences.

4.4 Discussion

This paper describes an innovative method to obtain the pose of the femur from single or biplane fluoroscopies to be used in knee tracking for accurate planning of orthopaedic surgery, starting from a patient specific model (obtained from volumetric dataset) or from a generic SSM. In the latter case, the radiation dose for the patient can be reduced. Knowing knee kinematics allows understanding pain zones associated with tensions of the ligaments and contact of the bones on each other, improving the outcome of the surgery.

Our registration method is based on GMMs and solves the Maximum Likelihood (ML) problem using an ECM approach, which allows significantly reducing the computational costs. Only a few seconds per image are enough to ensure the convergence of the system to the correct result, while for the previous methods [11, 67] several hours were needed

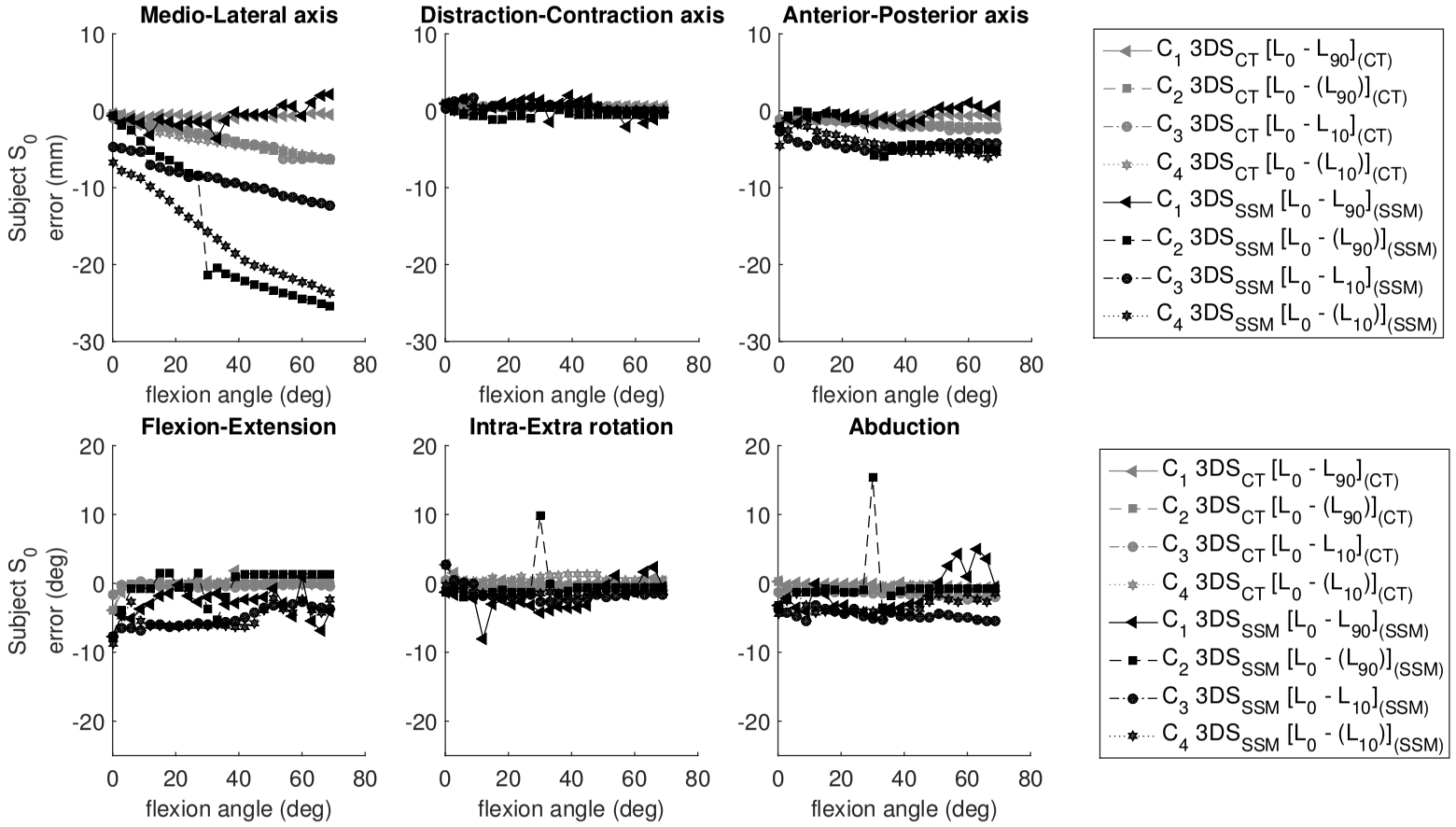

Figure 4.5: *Translation and rotation error of* $\mathbf{T}_{residual}$ *for* S_0

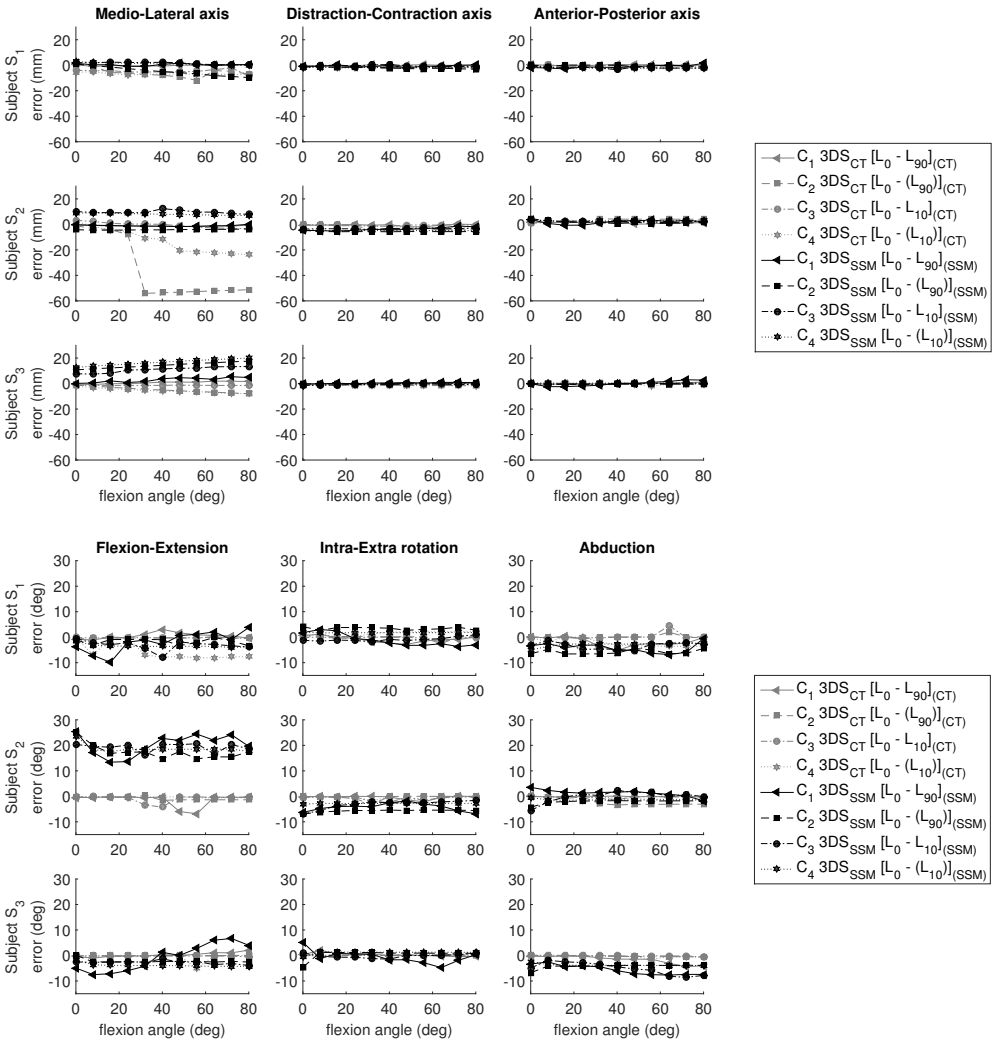

Figure 4.6: *Translation and rotation error of* $\mathbf{T}_{residual}$ *for* S_1, S_2, S_3

.

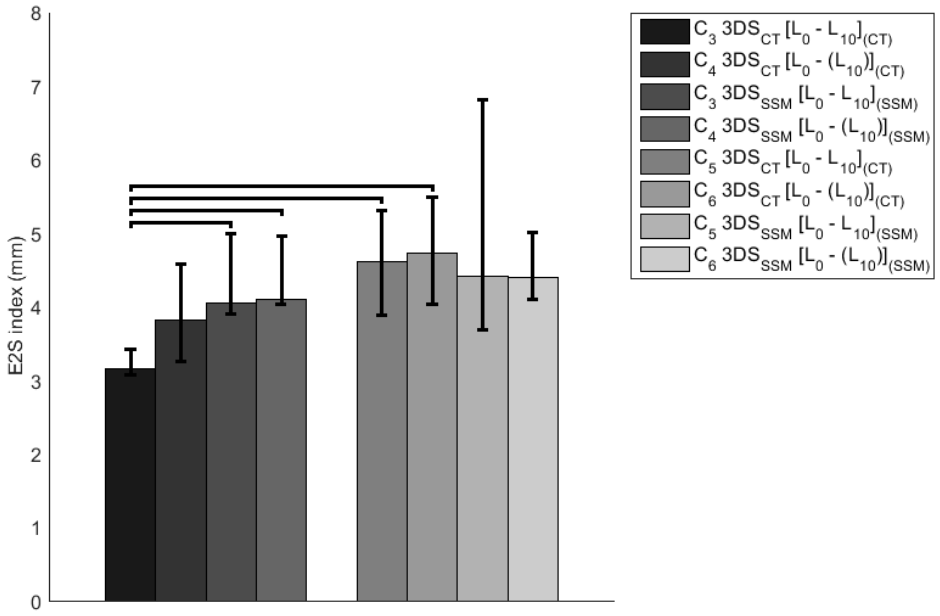

Figure 4.7: *Comparison of the Edge to Surface index for subjects S_1, S_2, S_3 with DRR or fluoroscopic images*

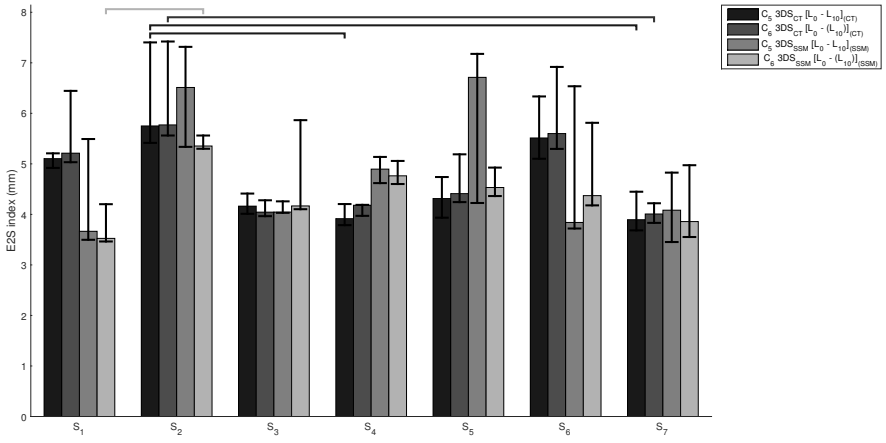

Figure 4.8: *Edge to Surface index for each subject with fluoroscopic images*

to reach convergence. Compared to previous works that used GMMs to register two different shapes on each other [21, 43, 73], our approach implements a 2D/3D registration, addressing the problem of a registration between two datasets with different dimensions. The method works in a semi-automatic way: it requires a rough initialization from the user and a threshold parameter to extract the contours with a Canny edge detector, saving time and improving the accuracy.

The results presented in our analysis show that the difference between the SSM and the CT extracted shape is significant only in a few cases, especially with diseased shapes. This can be due to limited morphing capability of the statistical model given by the low number (24) of healthy knees used as datasets [67].

Overall, the implemented registration method proved to have results comparable to the literature. In [13] the authors found a translation error of a few mm (0.48-0.81 for the median accuracy, and approximately 2 mm for the precision), that are comparable with the results we found in our experiments in the case of DRR tracking with S_0 and C_1.

The fluoroscopic images projection angle influences the tracking accuracy of the depth dimension. The ML axis has bigger errors compared to the others axis, because reducing the angle between the two projections from 90° to 10° decreases the pose determination accuracy [37]. The same behaviour regarding out of plane errors, can be observed when the tracking is performed with single-plane fluoroscopy. The error in depth increases from frame to frame, as there are no constraints on this axis. In the case of diseased patients, the error in depth can reach up to 6 cm (Figure 4.6). In fact, the uncertainty given by the single projection must be added to the non-perfect correspondence between the extracted contours and the statistical shape. The same considerations could be asserted relative to the rotation errors. A-part from Subject S_2, which has a very distal cut of the diaphysis (due to a tight joint intraoperatively) that compromises the reconstruction of the correct pose, the results are in line with those presented in [7, 63], who found errors below 1 cm with a higher distance in the out-of-plane axis.

The evaluation of the accuracy with fluoroscopic images was performed using the E2S index to allow an evaluation of the accuracy without knowing the correct pose of the ground truth. The results show a

statistical difference in the case of tracking with the 3DS_{CT} (Figure 4.7). This is probably due to a different Canny threshold, which influenced the correct positioning of the shape. The same error is not visible in the case of 3DS_{SSM} thanks to the lower deformation of the shape. These results are comparable with the ones stated by [13] who found an error of approximately 2 mm. However, their dataset had a bigger part of the shaft included in the images and in the shapes, augmenting the accuracy of the algorithm. Dealing with pathological subjects is more challenging, especially with a reduced set of shapes that created the SSM. Results are in the order of some mm (depending on the condition) and could be still acceptable to evaluate the kinematics of the knee. The method proved to be robust and efficient, especially when used with patient specific shapes. For single image tracking higher constraints on the depth axis must be implemented (e.g. a constrained motion of max 1 mm between frames). Future work will increase the number of shapes to construct the SSM and include also the tibia in the study, in order to have the joint angle value for a proper kinematic analysis. The easiest way to incorporate the tibia in the study is to treat femur and tibia as two different objects with specific deformable shape. In this case the optimization will be done for each object separately and the resulting pose in the common reference frame (the absolute reference frame) could be related to get the joint angle. Otherwise, a study on the knee kinematics could be done considering the whole joint. Femur and tibia move relatively to each other, and this motion can be considered by a single pose registration for the femur in the space followed by a constrained positioning of the tibia with respect to the pose of the femur.

CHAPTER 5

Conclusions

The study herein presented describes two different algorithms to obtain femur kinematics representation in the 3D space. Both algorithms are based on fluoroscopies and a Statistical Shape Model (SSM), resulting in a totally non-invasive method. Fluoroscopic sequences of images are already used in clinics to evaluate the kinematics of pathologic knees before surgery. The use of a completely automatic method improves the skills of the surgeon, providing a tool that allows the visualization of the movement from any point of view and reduces the efforts for planning the intervention. The surgeon is thus relieved from the duty of manually reconstructing the knee kinematics, resulting in a faster and more accurate registration. The clinical applicability is confirmed by the complete non invasiveness of the method, that works with data already acquired by the clinicians for a more complete representation of the 3D motion.

This study paves the way to a more complex planning software, completely integrated with the operating room devices, that goes on with the patient from the diagnosis to the follow up of the operation. Some crucial points are however still open: the SSM database is too small to accurately represent all the different bones and types of deformation of a generic osteoarthritic patient. The dataset must be enlarged, both with

healthy subjects, to reinforce the average shape, and with diseased knees, to expand the variability of the deformations.

Other limits of the study are intrinsic limits of the software. The algorithm based on Genetic Algorithm (GA) does not have an execution time compatible with surgery, as the fluoroscopic study needs some hours to be processed. Recent changes in computer processor have enhanced the frequency and capability of the machines. The algorithm, as proposed in this thesis, was developed on a Matlab interface, which slows down the performances as it is based on an interpreted language. The code could however be converted to a C++ language, intrinsically faster. Performance of the machine on which the code runs can be enhanced using a GPU approach and parallelizing the computation of the point distances for the optimization. The same optimization could be done for the Gaussian Mixture Model (GMM) based algorithm. In this case, however, the optimization is not critical, as the time employed by the algorithm is just a few minutes.

Both algorithms, when used with SSMs, need the initialization performed with two images. In fact, the SSM does not take into consideration the dimension of the bone segment that can change from subject to subject. When the tracking is performed with a single image, shape scaling can be confused with the location on the out-of-plane axis. This problem is not present if the algorithm works with two images or if the shape is derived from a Computed Tomography (CT) segmentation, that does not need scaling and deformation.

As observed in the results, the contour extraction plays a critical role in the accuracy of the algorithm. It is in fact the observation that both algorithms use to approximate pose and shape of the model. It is currently performed with a semi-automatic process based on β-splines, that require a great amount of time and the attention of the surgeon to identify the correct path along the image. This step could be optimized and made automatic using a Canny edge detector. A graphical user interface has been developed in order to perform this task. The clinician can set the two thresholds on which the Canny edge detector is based. The selection is performed interactively, so that the user can choose the best middle way between a noisy and a complete contour. In this way, the path is detected by the canny edge detector, and the clinician must only check

the correctness of the result.

The initial standard deviation of the Gaussian Mixture, that is currently guessed by the user depending on the number of points and on the initial distance between the shape and the backprojected contour, could be optimized using a tuning criterion based on the same factors. A similar optimization can be performed for the radius of the spherical volume used to consider the outliers in the GMM based algorithm. Although not fundamental, these optimizations improve the convergence of the algorithm and thus the execution time of the software.

Overall both methods proved to be robust and accurate, even with the small limitations described in this chapter. The trials performed indicate that the methods could be used in clinics, to help the surgeon with the planning of the intervention. Future advancements will concern the complete analysis of the knee joint, including both tibia and patella in the 2D/3D registration. The SSM as presented in chapter 2 has been already built also for tibia and patella. The 2D/3D registration could be performed using the same software developed here and described in chapter 3 and in chapter 4. The presentation to the clinicians, however, must be done through a graphical user interface, easy to use and immediate to understand. The developed software could then become a valid tool that can help the surgeon during pre-operative planning. All the steps will be clearly explained and the parameters can be changed in real time. Thanks to the velocity of the algorithm, numerous trials could be performed with different parameters. The surgeon can thus have a smart software able to adapt to different cases, which uses standard clinical exams already performed in the routine and elaborates them at nearly no cost.

Bibliography

[1] Arthritis.org. http://http://www.arthritis.org. Accessed: 2015-08-27.

[2] Brainlab.com. http://http://www.brainlab.com. Accessed: 2015-08-27.

[3] Oecd library. http://www.oecd-ilibrary.org/. Accessed: 2015-08-05.

[4] Radiologyinfo.org. http://www.radiologyinfo.org. Accessed: 2015-06-05.

[5] Stryker.com. http://http://www.stryker.com. Accessed: 2015-08-27.

[6] Zimmer.com. http://http://www.zimmer.com. Accessed: 2015-08-27.

[7] S Acker, R Li, H Murray, PS John, S Banks, S Mu, U Wyss, and K Deluzio. Accuracy of single-plane fluoroscopy in determining relative position and orientation of total knee replacement components. *Journal of Biomechanics*, 44(4):784–787, 2011.

[8] M Akbari Shandiz. *Component Placement in Hip and Knee Replacement Surgery: Device Development, Imaging and Biomechanics*. PhD thesis, Biomedical Engineering, 2015.

[9] W. Anderst, R. Zauel, J. Bishop, E. Demps, and S. Tashman. Validation of three-dimensional model-based tibio-femoral tracking during running. *Medical Engineering & Physics*, 31(1):10–16, 2009.

[10] K S Arun, T S Huang, and S D Blostein. Least-squares fitting of two 3-d point sets. *Pattern Analysis and Machine Intelligence, IEEE Transactions on*, (5):698–700, 1987.

[11] N Baka, M de Bruijne, T van Walsum, BL Kaptein, JE Giphart, M Schaap, WJ Niessen, and BPF Lelieveldt. Statistical shape model-based femur kinematics from biplane fluoroscopy. *Medical Imaging, IEEE Transactions on*, 31(8):1573–1583, 2012.

[12] N Baka, BL Kaptein, M de Bruijne, T van Walsum, JE Giphart, WJ Niessen, and BPF Lelieveldt. 2d–3d shape reconstruction of the distal femur from stereo x-ray imaging using statistical shape models. *Medical Image Analysis*, 15(6):840–850, 2011.

[13] N Baka, BL Kaptein, JE Giphart, M Staring, M de Bruijne, BPF Lelieveldt, and E Valstar. Evaluation of automated statistical shape model based knee kinematics from biplane fluoroscopy. *Journal of Biomechanics*, 47(1):122–129, 2014.

[14] E Beretta, E De Momi, V Camomilla, A Cereatti, A Cappozzo, and G Ferrigno. Hip joint centre position estimation using a dual unscented kalman filter for computer-assisted orthopaedic surgery. *Proceedings of the Institution of Mechanical Engineers, Part H: Journal of Engineering in Medicine*, 228(9):971–982, 2014.

[15] E. Beretta, M. Valenti, E. De Momi, and G. Ferrigno. Hip joint center location with kalman filter. *Journal of Bone & Joint Surgery, British Volume*, 94-B(SUPP XLIV):68, 2012.

[16] PJ Besl and ND McKay. Method for registration of 3-d shapes. In *Robotics-DL tentative*, pages 586–606. International Society for Optics and Photonics, 1992.

[17] JWJ Bijlsma and K Knahr. Strategies for the prevention and management of osteoarthritis of the hip and knee. *Best Practice & Research Clinical Rheumatology*, 21(1):59–76, 2007.

[18] AD Brett and CJ Taylor. A method of automated landmark generation for automated 3d pdm construction. *Image and Vision Computing*, 18(9):739–748, 2000.

[19] J Canny. A computational approach to edge detection. *Pattern Analysis and Machine Intelligence, IEEE Transactions on*, (6):679–698, 1986.

[20] A Cappozzo, F Catani, U Della Croce, and A Leardini. Position and orientation in space of bones during movement: anatomical frame definition and determination. *Clinical Biomechanics (Bristol, Avon)*, 10(4):171–178, June 1995.

[21] H Chui and A Rangarajan. A new point matching algorithm for non-rigid registration. *Computer Vision and Image Understanding*, 89(2):114–141, 2003.

[22] TF Cootes, DH Cooper, CJ Taylor, and J Graham. A trainable method of parametric shape description. In *BMVC91*, pages 54–61. Springer, 1991.

[23] TF Cootes, DH Cooper, CJ Taylor, and J Graham. Trainable method of parametric shape description. *Image and Vision Computing*, 10(5):289–294, 1992.

[24] TF Cootes, GJ Edwards, and CJ Taylor. Active appearance models. *IEEE Transactions on Pattern Analysis and Machine Intelligence*, 23(6):681–685, 2001.

[25] TF Cootes, MC Ionita, C Lindner, and P Sauer. Robust and accurate shape model fitting using random forest regression voting. In *Computer Vision–ECCV 2012*, pages 278–291. Springer, 2012.

[26] TF Cootes and CJ Taylor. Active shape models - smart snakes. In *BMVC92*, pages 266–275. Springer, 1992.

[27] TF Cootes, CJ Taylor, DH Cooper, and J Graham. Active shape models-their training and application. *Computer Vision and Image Understanding*, 61(1):38–59, 1995.

[28] IG Costa Filho. *Mixture Models for the Analysis of Gene Expression: Integration of Multiple Experiments and Cluster Validation*. PhD thesis, Freie Universität Berlin, 2008.

[29] P Creamer and MC Hochberg. Osteoarthritis of the knee. *The Lancet*, 350(9087):1328, 1997.

[30] RH Davies, CJ Twining, TF Cootes, JC Waterton, and CJ Taylor. 3d statistical shape models using direct optimisation of description length. In *Computer Vision – ECCV 2002*, pages 3–20. Springer, 2002.

[31] L Davis. *Handbook of genetic algorithms*, volume 115. Van Nostrand Reinhold New York, 1991.

[32] E De Momi, E Beretta, and G Ferrigno. Hip joint centre localisation with an unscented kalman filter. *Computer Methods in Biomechanics and Biomedical Engineering*, 16(12):1319–1329, 2013.

[33] AP Dempster, NM Laird, and DB Rubin. Maximum likelihood from incomplete data via the em algorithm. *Journal of the Royal Statistical Society. Series B (methodological)*, pages 1–38, 1977.

[34] D Dennis, MR Mahfouz, RD Komistek, and W Hoff. In vivo determination of normal and anterior cruciate ligament-deficient knee kinematics. *Journal of Biomechanics*, 38(2):241–53, February 2005.

[35] CE Draper, JM Santos, LC Kourtis, TF Besier, M Fredericson, GS Beaupre, GE Gold, and SL Delp. Feasibility of using real-time mri to measure joint kinematics in 1.5 t and open-bore 0.5 t systems. *Journal of Magnetic Resonance Imaging*, 28(1):158–166, 2008.

[36] M Fadda, D Bertelli, S Martelli, M Marcacci, P Dario, C Paggetti, D Caramella, and D Trippi. Computer assisted planning for total knee arthroplasty. In *CVRMed-MRCAS'97*, pages 617–628. Springer, 1997.

[37] G. Ferrigno and A. Pedotti. Opto-electronics based systems. In P Allard, I A Stokes, and J P Bianchi, editors, *Three-Dimensional Analysis of Human Movement, Human Kinetics 1st ed*, pages 57–78. Human Kinetics Publishers, 1995.

[38] M Fleute and S Lavallée. Nonrigid 3-d/2-d registration of images using statistical models. In *Medical Image Computing and Computer-Assisted Intervention–MICCAI'99*, pages 138–147. Springer, 1999.

[39] T Heimann, I Wolf, T Williams, and HP Meinzer. 3d active shape models using gradient descent optimization of description length. In *Information Processing in Medical Imaging*, pages 566–577. Springer, 2005.

[40] J Henckel, R Richards, K Lozhkin, S Harris, FM Rodriguez y Baena, ARW Barrett, and JP Cobb. Very low-dose computed tomography for planning and outcome measurement in knee replacement the imperial knee protocol. *Journal of Bone & Joint Surgery, British Volume*, 88(11):1513–1518, 2006.

[41] KCT Ho, SK Saevarsson, H Ramm, R Lieck, S Zachow, GB Sharma, EL Rex, S Amiri, BCY Wu, A Leumann, et al. Computed tomography analysis of knee pose and geometry before and after total knee arthroplasty. *Journal of Biomechanics*, 45(13):2215–2221, 2012.

[42] JP Holden, JA Orsini, KL Siegel, and TM Kepple. Surface movement errors in shank kinematics and knee kinetics during gait. *Gait & Posture*, 5:217–227, 1997.

[43] R Horaud, F Forbes, M Yguel, G Dewaele, and J Zhang. Rigid and articulated point registration with expectation conditional maximization. *Pattern Analysis and Machine Intelligence, IEEE Transactions on*, 33(3):587–602, 2011.

[44] M Juneja and PS Sandhu. Performance evaluation of edge detection techniques for images in spatial domain. *International Journal of Computer Theory and Engineering*, 1(5):614–621, 2009.

[45] J Kittler. On the accuracy of the sobel edge detector. *Image and Vision Computing*, 1(1):37–42, 1983.

[46] HW Kuhn. The hungarian method for the assignment problem. *Naval research logistics quarterly*, 2(1-2):83–97, 1955.

[47] A Leardini, L Chiari, U Della Croce, and A Cappozzo. Human movement analysis using stereophotogrammetry. part 3. soft tissue artifact assessment and compensation. *Gait & Posture*, 21(2):212–25, February 2005.

[48] C Lindner, S Thiagarajah, J Wilkinson, The Consortium, G Wallis, and Timothy F Cootes. Fully automatic segmentation of the proximal femur using random forest regression voting. *IEEE Transactions on Medical Imaging*, 32(8):1462–1472, 2013.

[49] A Litwic, MH Edwards, EM Dennison, and C Cooper. Epidemiology and burden of osteoarthritis. *British Medical Bulletin*, page lds038, 2013.

[50] WE Lorensen and HE Cline. Marching cubes: A high resolution 3d surface construction algorithm. In *ACM Siggraph Computer Graphics*, volume 21, pages 163–169. ACM, 1987.

[51] J Bohannon Mason, Thomas K Fehring, Rhonda Estok, Deirdre Banel, and Kyle Fahrbach. Meta-analysis of alignment outcomes in computer-assisted total knee arthroplasty surgery. *The Journal of arthroplasty*, 22(8):1097–1106, 2007.

[52] CT Metz. Digitally reconstructed radiographs. *Utrecht: Utrecht University*, page 79, 2005.

[53] DL Miranda, MJ Rainbow, EL Leventhal, JJ Crisco, and BC Fleming. Automatic determination of anatomical coordinate systems for three-dimensional bone models of the isolated human knee. *Journal of Biomechanics*, 43(8):1623–1626, 2010.

[54] BC Munsell, P Dalal, and S Wang. Evaluating shape correspondence for statistical shape analysis: A benchmark study. *Pattern Analysis and Machine Intelligence, IEEE Transactions on*, 30(11):2023–2039, 2008.

[55] S Okamoto, H Mizu-uchi, K Okazaki, S Hamai, Y Tashiro, H Nakahara, and Y Iwamoto. Two-dimensional planning can result in internal rotation of the femoral component in total knee arthroplasty. *Knee Surgery, Sports Traumatology, Arthroscopy*, pages 1–7, 2014.

[56] F Paternostre, PE Schwab, and E Thienpont. The difference between weight-bearing and non-weight-bearing alignment in patient-specific instrumentation planning. *Knee Surgery, Sports Traumatology, Arthroscopy*, 22(3):674–679, 2014.

[57] GB Sharma, SK Saevarsson, S Amiri, S Montgomery, H Ramm, DD Lichti, R Lieck, S Zachow, and C Anglin. Radiological method for measuring patellofemoral tracking and tibiofemoral kinematics before and after total knee replacement. *Bone and Joint Research*, 1(10):263–271, 2012.

[58] CW Spoor and FE Veldpaus. Rigid body motion calculated from spatial co-ordinates of markers. *Journal of Biomechanics*, 13(4):391–393, 1980.

[59] MA Styner, KT Rajamani, LP Nolte, G Zsemlye, G Székely, CJ Taylor, and RH Davies. Evaluation of 3d correspondence methods for model building. In *Information processing in medical imaging*, pages 63–75. Springer, 2003.

[60] TSY Tang, NJ MacIntyre, and HS Gill. Accuracy of a fluoroscopy technique for assessing patellar tracking. *Medical Image Computing and Computer-Assisted Intervention - MICCAI 2003*, 2003.

[61] S. Tashman. Abnormal rotational knee motion during running after anterior cruciate ligament reconstruction. *American Journal of Sports Medicine*, 32(4):975–983, April 2004.

[62] S Tashman and W Anderst. In-vivo measurement of dynamic joint motion using high speed biplane radiography and CT: Application to canine ACL deficiency. *Journal of Biomechanical Engineering*, 125(2):238, 2003.

[63] L Tersi, A Barré, S Fantozzi, and R Stagni. In vitro quantification of the performance of model-based mono-planar and bi-planar fluoroscopy for 3d joint kinematics estimation. *Medical & Biological Engineering & Computing*, 51(3):257–265, 2013.

[64] HH Thodberg. Minimum description length shape and appearance models. In *Information Processing in Medical Imaging*, pages 51–62. Springer, 2003.

[65] TY Tsai, TW Lu, CM Chen, MY Kuo, and HC Hsu. A volumetric model-based 2d to 3d registration method for measuring kinematics of natural knees with single-plane fluoroscopy. *Medical Physics*, 37(3):1273–1284, 2010.

[66] M Valenti, C Chen, E De Momi, G Ferrigno, and G Zheng. 3d shape landmark correspondence by minimum description length and local linear regularization. In *XIII Mediterranean Conference on Medical and Biological Engineering and Computing 2013*, pages 1837–1840. Springer, 2014.

[67] M Valenti, E De Momi, W Yu, G Ferrigno, M Akbari Shandiz, C Anglin, and G Zheng. Fluoroscopy-based tracking of femoral kinematics with statistical shape models. *International Journal of Computer Assisted Radiology and Surgery*, pages 1–9, 2015.

[68] M Valenti, E De Momi, W Yu, G Ferrigno, and G Zheng. 2d/3d SSM reconstruction method based on robust point matching. *Bone & Joint Journal Orthopaedic Proceedings Supplement*, 96(SUPP 16):1–1, 2014.

[69] S Wang, T Kubota, and T Richardson. Shape correspondence through landmark sliding. In *Computer Vision and Pattern Recognition, 2004. CVPR 2004. Proceedings of the 2004 IEEE Computer Society Conference on*, volume 1, pages I–143. IEEE, 2004.

[70] J Xie and PA Heng. Shape modeling using automatic landmarking. In *Medical Image Computing and Computer-Assisted Intervention–MICCAI 2005*, pages 709–716. Springer, 2005.

[71] W Yu and G Zheng. Personalized x-ray reconstruction of the proximal femur via a new control point-based 2d-3d registration and residual complexity minimization. In *Eurographics Workshop on Visual Computing for Biology and Medicine, VCBM 2014, Vienna, Austria, 2014. Proceedings*, pages 155–162, 2014.

[72] W Zhang, RW Moskowitz, G Nuki, S Abramson, RD Altman, N Arden, S Bierma-Zeinstra, KD Brandt, P Croft, M Doherty, et al. OARSI recommendations for the management of hip and knee osteoarthritis, part i: critical appraisal of existing treatment guidelines and systematic review of current research evidence. *Osteoarthritis and Cartilage*, 15(9):981–1000, 2007.

[73] G Zheng. Expectation conditional maximization-based deformable shape registration. In *Computer Analysis of Images and Patterns*, pages 548–555. Springer, 2013.

[74] G Zheng, X Dong, KT Rajamani, X Zhang, M Styner, RU Thoranaghatte, LP Nolte, and MG Ballester. Accurate and robust reconstruction of a surface model of the proximal femur from sparse-point data and a dense-point distribution model for surgical navigation. *IEEE transactions on Bio-Medical Engineering*, 54(12):2109–22, December 2007.

[75] G Zheng, S Gollmer, S Schumann, X Dong, T Feilkas, and MAG Ballester. A 2d/3d correspondence building method for reconstruction of a patient-specific 3d bone surface model using point distribution models and calibrated x-ray images. *Medical Image Analysis*, 13(6):883–899, 2009.

[76] Z Zhu and G Li. An automatic 2d–3d image matching method for reproducing spatial knee joint positions using single or dual fluoroscopic images. *Computer Methods in Biomechanics and Biomedical Engineering*, 15(11):1245–1256, 2012.